

# Synergistic Effects of The Hybridization Between Boron-Doped Carbon Quantum Dots And n/n-Type g-C<sub>3</sub>N<sub>4</sub> Homojunction For Boosted Visible-Light Photocatalytic Activity

**Sue Jiun Phang**

Heriot-Watt University - Malaysia Campus

**Jiale Lee**

Monash University Sunway Campus: Monash University Malaysia

**Voon-Loong Wong**

Heriot-Watt University - Malaysia Campus

**Lling-Ling Tan** (✉ [tan.lingling@monash.edu](mailto:tan.lingling@monash.edu))

Monash University - Malaysia Campus

**Siang-Piao Chai**

Monash University - Sunway Campus: Monash University Malaysia

---

## Research Article

**Keywords:** Photocatalysis, boron, carbon quantum dots, graphitic carbon nitride, homojunction, wastewater treatment

**Posted Date:** September 15th, 2021

**DOI:** <https://doi.org/10.21203/rs.3.rs-834440/v1>

**License:**  This work is licensed under a Creative Commons Attribution 4.0 International License.  
[Read Full License](#)

---

**Version of Record:** A version of this preprint was published at Environmental Science and Pollution Research on January 28th, 2022. See the published version at <https://doi.org/10.1007/s11356-021-18253-0>.

# Abstract

Carbon quantum dots (CQDs) are particularly sought after for their highly tailorable photoelectrochemical and optical properties. Simultaneously, graphitic carbon nitride (g-C<sub>3</sub>N<sub>4</sub>) has also gained widespread attention due to its suitable band gap energy as well as excellent chemical and thermal stabilities. Herein, a novel boron-doped CQD (BCQD) hybridized g-C<sub>3</sub>N<sub>4</sub> homojunction (CN) nanocomposite was rationally engineered and fabricated via a facile hydrothermal route. The optimal photocatalyst sample, 1-BCQD/CN (with a 1:3 mass ratio of boron to CQD) accomplished a Rhodamine B (RhB) degradation efficiency of 97.0 % within 4 hours under low-powered LED light irradiation. The kinetic rate constant of  $1.39 \times 10^{-2} \text{ min}^{-1}$  achieved by the optimum sample was found to be 3.6- and 2.8-folds higher than that of pristine CN and un-doped CQD/CN, respectively. Furthermore, 1-BCQD/CN demonstrated remarkable stability, where it retained close to 99.0% of its initial photocatalytic efficiency after three consecutive cycles. The marked improvement in photocatalytic performance of 1-BCQD/CN was attributed to several concomitant factors such as enhanced electron migration from CN to BCQD, suppressed electron-hole recombination and significantly higher charge density in facilitating charge migration. Based on the scavenging tests, it was revealed that the photogenerated holes (h<sup>+</sup>), superoxide anions ( $\bullet\text{O}_2^-$ ) and hydroxyl radicals ( $\bullet\text{OH}$ ) were the primary reactive species responsible for the photodegradation process. Overall, the highly efficient 1-BCQD/CN composite with excellent photocatalytic activity could provide a cost-effective and robust means for addressing the increasing concerns over global environmental pollution.

## Introduction

In the recent years, the dramatic growth in global population calls for immediate measures to protect the environment and natural resources. While the rapid industrialization has indeed promoted the blooming of various sectors including food and beverage, paper and textile, irrigation and drainage, medical and pharmaceutical, etc., these industries are accountable for several major environmental issues. In this regard, the discharge of effluents by these production and manufacturing plants is detrimental to Mother Nature, resulting in the pollution of water resources and diminished water quality. Notably, the level of dissolved contaminants in the vast majority of water bodies is above the acceptable standard for human consumption, leading to the scarcity of clean water in many communities around the world. Based on data from the World Health Organization, an annual estimation of 485,000 diarrheal deaths occur due to the consumption of contaminated drinking water while waterborne diseases such as cholera, polio and typhoid remain as serious threats to the public health (Organization, 2019). Besides the adverse impact on human health, water pollution also contributes to eutrophication in lakes and the destruction of aquatic ecosystems. Therefore, an effective, sustainable and environmentally-benign method to treat polluted water is of utmost importance.

Photocatalysis has garnered widespread attention amongst researchers as this cutting-edge technology is highly green and sustainable. While water treatment by means of photo-driven reactions is undoubtedly

environmentally friendly, the performances of the existing photocatalytic systems are greatly hampered by several setbacks. Among the prominent issues include the ineffective utilization of solar energy and the rapid recombination rate of electron-holes pairs (Weon et al., 2019; Jiao et al., 2020). As visible light makes up an approximately 42 % of the solar energy, the design of a visible-light-responsive photocatalyst is greatly desired due to its relatively high photonic energy (Wang et al., 2017c). Hitherto, most of the existing photocatalytic systems are only active under high energy ultraviolet (UV) light which constitutes merely 6 % of the entire solar spectrum (An et al., 2016). A number of strategies such as functionalization, elemental doping and size tuning have been proposed to boost the apparent quantum efficiency of the existing photocatalysts and concurrently diminish the aforementioned limitations (Nassar and Abdelrahman, 2017; Ma et al., 2018; Li et al., 2020b). A plethora of nanomaterials have also been identified as promising photocatalytic materials. These include metallic titanium oxide ( $\text{TiO}_2$ ), tungsten oxide ( $\text{WO}_3$ ), MXenes as well as non-metallic CQDs, graphitic carbon nitride ( $\text{g-C}_3\text{N}_4$ ), phosphorus (P), graphene and combinations hereof (Cushing et al., 2017; Cao et al., 2018; Jeevitha et al., 2018; Hu et al., 2019; Kooshki et al., 2019; Mishra et al., 2019).

Ascribing to its suitable electronic band structure, facile synthesis and readily tunable features, two-dimensional (2D)  $\text{g-C}_3\text{N}_4$  has thrust into the limelight within the field of photocatalysis (Che et al., 2019). As compared to its metal-based counterparts, the metal-free  $\text{g-C}_3\text{N}_4$  has also alleviated the risk of metal-leaching, which is known to be a process where toxic metal components dissolve into liquid medium, inflicting detrimental damage to the environment (Zhang et al., 2016b; Sahu et al., 2020). The vast untapped potential of  $\text{g-C}_3\text{N}_4$  has prompted much research interests in studying its structural framework, optoelectronic and physicochemical properties. Among the more effective strategies in enhancing the photocatalytic performance of  $\text{g-C}_3\text{N}_4$  is through the formation of a homojunction system, where the difference in conduction band (CB) and valence band (VB) levels between precursors could facilitate the separation of photoinduced charge carriers (Phang et al., 2020b). Several research articles on  $\text{g-C}_3\text{N}_4$  homojunction with enhanced photocatalytic performance have been published in literature (Ye et al., 2017; Phang et al., 2020a). For instance, Tan et al. successfully fabricated a mesoporous  $\text{g-C}_3\text{N}_4$  nanosheets laminated homojunction, which displayed a 12.5- and 6.5-fold improvement in performance as compared to pristine  $\text{g-C}_3\text{N}_4$  derived from melamine and amino cyanamide respectively (Tan et al., 2017). Similarly, Yang's group constructed a triazine-/heptazine-based  $\text{g-C}_3\text{N}_4$  homojunction via the overgrowth of triazine-based  $\text{g-C}_3\text{N}_4$  nanoparticles embedded on the inner wall of the heptazine-based  $\text{g-C}_3\text{N}_4$  hollow tubes (Yang et al., 2020). The efficiency for photocatalytic  $\text{H}_2$  generation was drastically improved, with a  $\text{H}_2$  evolution rate 12-times higher in relative to bulk  $\text{g-C}_3\text{N}_4$ . On the whole, the ameliorated photoactivities in different applications are primarily credited to the enhanced photo-response towards visible light, rapid charge transfer and separation in addition to excellent photo-stability upon the formation of homojunction structures.

To further improve the photoactivity of  $\text{g-C}_3\text{N}_4$ , the doping of a co-catalyst onto the fundamental framework is regarded as one of the most effective strategies (Ran et al., 2015; Chen et al., 2017; Hasija

et al., 2019). Carbon quantum dots (CQDs) are widely perceived as a novel class of nanomaterials with ultrafine dimensions of less than 10 nm (Phang and Tan, 2019). CQDs have become the focus of attention among material scientists and researchers in the recent years owing to their prominent optical and physicochemical properties. Furthermore, CQDs are also highly sought after for its up-converted photoluminescence (UCPL) properties, extended range of sensitivity towards visible light as well as its inexpensive synthesis cost (Wang et al., 2019a; Molaei, 2020). The readily tunable features of CQDs, chemically and physically, renders their robustness and allow them to be tailored precisely for a variety of applications. Recently, there has been a surge in publications on the modification strategies of CQDs to further enhance their photocatalytic effectiveness. These strategies include size tuning for quantum confinement effect (Li and Zhao, 2014), surface passivation and functionalization (Luo et al., 2013; Lim et al., 2015; Yang et al., 2016; Pan et al., 2017), heteroatom doping and the formation of hybridized nanocomposites (Ma et al., 2016; Zhang et al., 2017a). Among the common doping elements for CQDs are nitrogen (N), boron (B), sulfur (S), phosphorus (P), which are typically derived from urea, boric acid,  $\alpha$ -cysteine and phosphoric acid, respectively (Bhati et al., 2019; Lin et al., 2019; Wang et al., 2019b; Zhang et al., 2020b). Each element has its distinctive advantages over the other elements in improving the photoactivity of CQDs. For instance, N-doped CQDs were reported to increase the aqueous dispersibility and fluorescence emission of the composite while B-doped CQDs displayed enhanced visible light absorption and quantum yield (Ma et al., 2012; Guo et al., 2018; Song et al., 2020). On the other hand, doping of heteroatom S was shown to improve the electrical conductivity of CQDs whereas the introduction of P dopants accelerated the electron transfer to impede charge carrier recombination (Wang et al., 2019b; Zhang et al., 2020c). Collectively, it is apparent that the doping of CQDs with different heteroatoms are promising to drastically enhance various extrinsic properties and structural features advantageous for photocatalysis. For instance, Peng et al. successfully fabricated the B-doped carbon dots via a simple hydrothermal route. Based on the photoactivity test over RhB and methylene blue (MB) degradation. The synthesized B-doped carbon dots demonstrated an outstanding performance in which a 100% degradation of both dyes were attained within a short span of 170 minutes (Peng et al., 2020).

In this work, we report the smart engineering of zero-dimensional (0D) B-doped CQD (BCQD) on 2D g-C<sub>3</sub>N<sub>4</sub>/g-C<sub>3</sub>N<sub>4</sub> homojunction (CN) to form a highly robust hybrid BCQD/CN. To the best of our knowledge, the fabrication of this novel and efficient nanocomposite system for RhB degradation has not been reported in literature thus far. Herein, BCQDs were doped onto CN via a facile hydrothermal method. The CQDs were derived from citric acid with boric acid as the B-dopant, while g-C<sub>3</sub>N<sub>4</sub> homojunctions were fabricated with urea and thiourea as the precursors. The mass loadings of boric acid were varied to determine the optimum amount of B-dopant over the n/n-junctioned g-C<sub>3</sub>N<sub>4</sub>. The photocatalytic efficiency of the as-developed photocatalyst samples were evaluated via the degradation of RhB dye. It is noteworthy that the present work employs the use of a low-powered 18 W LED light as the irradiation source, rendering the overall photocatalytic process both environmentally benign and economically feasible. All in all, this study aims to provoke novel research ideas in the field of photocatalysis with the development of BCQDs incorporated g-C<sub>3</sub>N<sub>4</sub>/g-C<sub>3</sub>N<sub>4</sub> homojunction nanocomposites.

# Experimental

## 2.1 Materials

Citric acid (99.5 %, MW = 192.12 g/mol), urea (99.5 %, MW = 60.06 g/mol), thiourea (98%, MW = 76.12 g/mol) and p-benzoquinone (BZQ, 98 %, MW = 108.10 g/mol) were purchased from R&M Chemicals, UK. Boric acid (99.5 %, MW = 61.83 g/mol) was purchased from Merck KGaA, Germany. Rhodamine B dye (RhB, 98.5 %, MW = 479.02 g/mol, pKa = 4.2), triethanolamine (TEOA, 99 %, MW = 149.19 g/mol) and 2-propanol (IPA, 99 %, MW = 60.1 g/mol) were obtained from QReC (Asia) Sdn. Bhd., Malaysia. Distilled water was employed throughout the experiments. All reagents were of analytical grade (AR) and applied without further purification.

## 2.2 Preparation of photocatalysts

### 2.2.1 Synthesis of BCQD

Three (3) grams of citric acid and  $x$ -amount of boric acid were mixed in 15 ml of distilled water followed by mild stirring for 10 min. The symbol ' $x$ ' denotes the amount of boron-dopant employed (0.5, 1, 2 and 3 g) in the synthesis of BCQDs with respect to a fixed amount of CQDs. The homogeneous mixture was then transferred into a Teflon-lined autoclave reactor for hydrothermal treatment at 180°C for 14 hrs, after which the solution was cooled naturally to ambient temperature. Subsequently, the resultant brown suspension was subjected to centrifugation at 12,000 rpm for 20 min to remove larger particles and impurities. The supernatant containing purified BCQD was obtained and dried in an oven at 90°C overnight before further use. The prepared samples with 0.5, 1, 2 and 3 g of boric acid were denoted as 0.5-BCQD, 1-BCQD, 2-BCQD and 3-BCQD respectively. Pristine CQD samples were also synthesized following a similar procedure without the addition of boric acid.

### 2.2.2 Synthesis of g-C<sub>3</sub>N<sub>4</sub>/g-C<sub>3</sub>N homojunction (CN)

g-C<sub>3</sub>N<sub>4</sub>/g-C<sub>3</sub>N<sub>4</sub> homojunction was prepared by a facile thermal polymerization route following a reported work with slight modifications (Phang et al., 2020a). Typically, 6 g of each precursor (urea and thiourea) were mixed in 30 ml of distilled water with gentle stirring to obtain a well-mixed solution. Subsequently, the resultant mixture was placed in the oven at 90°C overnight to construct the nanocomposite photocatalyst. The molecular composite was transferred into a porcelain crucible and subjected to calcination at 550°C with a ramping rate of 2°C/min for 2 hrs. The resultant yellow-colored solid was cooled to ambient temperature overnight and then ground to fine powders before further use.

### 2.2.3 Synthesis of BCQD/CN nanocomposite

One (1) gram of the as-synthesized CN and 0.01 g (1 wt %) of pristine CQD or  $x$ -BCQD were mixed in 90 ml and 10 ml of distilled water respectively. The two solutions undergone ultrasonication in separate beakers for 30 min to minimize agglomeration and exfoliate the layers of g-C<sub>3</sub>N<sub>4</sub> nanosheets. Next, both solutions were mixed and stirred for 30 min. The resultant beige-colored solution was transferred into a

Teflon-lined autoclave reactor and heated at 120°C for 4 hrs. The sample was collected via filtration and washed with distilled water several times. Finally, the nanocomposite photocatalyst was obtained after oven-drying at 70 °C overnight. The final photocatalyst samples were labelled as CQD/CN, 0.5-BCQD/CN, 1-BCQD/CN, 2-BCQD/CN and 3-BCQD/CN. The synthesis route of BCQD/CN nanocomposites is depicted in Fig. 1.

## 2.3 Characterization of materials

The surface morphology of CQD/CN and the optimized photocatalyst sample, 1-BCQD/CN were analyzed with transmission electron microscopy (TEM) (FEI Tecnai G2 20 S-TWIN, USA) by applying 200 kV of accelerating voltage. Field emission scanning electron microscope (FE-SEM) (ultra-high-resolution Hitachi SU8010, Japan) coupled with energy dispersive X-ray analyzer (EDX) were carried out to study the surface morphology, elemental compositions and framework of CN, CQD/CN and 1-BCQD/CN. The crystal structures of CN, CQD/CN and 1-BCQD/CN were characterized via high resolution X-ray diffraction (XRD) with X-ray diffractometer (Bruker D8 Discover, Germany) in the presence of Ni-filtered Cu K $\alpha$  operated at 40 kV and 40 mA, with 0.02 °/s as scanning rate. Fourier Transform Infrared (FTIR) spectra of CN, CQD/CN and 1-BCQD/CN were measured with FTIR spectrometer (Perkin Elmer Frontier). Ultraviolet-visible diffuse reflectance spectra (UV-vis DRS) of the as-developed photocatalyst samples were analyzed using Cary 100 UV-Vis (Agilent Technologies, USA). All optical evaluations were obtained at room temperature and pressure with a wavelength range of 300–800 nm. Photoluminescence (PL) spectra of the samples were recorded with fluorescence spectrometer (Perkin Elmer LS-55, USA) with 420 nm as measurement wavelength.

## 2.4 Photocatalytic activity evaluation

The photoactivity of as-prepared samples were assessed via the degradation of a cationic dye, Rhodamine B (RhB). The photocatalytic experiments were conducted in a homemade photoreactor under ambient conditions. Typically, 0.15 g of photocatalyst sample was uniformly distributed in a glass beaker containing 100 mL of 10 mg/L RhB solution. The resultant mixture was stirred without light for 30 min to establish adsorption-desorption equilibrium. Before switching on the light source, a 5 ml aliquot of the equilibrated RhB solution was collected and used as the blank sample. The LED lamp (4410R-18W) was then switched on as the source of irradiation and samples were obtained at every 60-min interval for a total duration of 240 min. The range of wavelength and intensity of LED light source employed are 400–700 nm and 0.237 W/m<sup>2</sup> respectively. All solution samples were subjected to centrifugation at 12,000 rpm for 3 mins for removal of suspended powdered photocatalyst. The supernatant was then obtained and measured using a UV-Vis spectrophotometer (Hach DR 6000) and a wavelength scan ranging from 300–800 nm was obtained. The characteristic peak of the absorption band for RhB dye (552 nm) was also recorded with respect to time. Pseudo first rate constant,  $k$  of the photo-reaction was determined following the Langmuir-Hinshelwood model as presented in Eq. 1, where  $C_0$  (mg/L),  $C$  (mg/L),  $k$  (min<sup>-1</sup>) and  $t$  (min) denote the RhB concentration at time  $t$ , initial concentration, kinetic rate constant and irradiation time, respectively.

$$\ln \frac{C_0}{C} = k \times t \quad (1)$$

The efficiency of as-synthesized photocatalyst samples was evaluated in accordance with Eq. 2:

$$DE = \frac{C_0 - C}{C_0} \times 100\%$$

Degradation efficiency, (2)

A standard equilibrium curve was constructed to establish a correlation between the absorbance and the concentration of RhB dye conforming to the Beer-Lambert Law, which proclaims that the concentration and absorption of a species in the solution is proportional to one another.

## 2.5 Photoelectrochemical measurement

Photoelectrochemical characterizations of the photocatalysts were analyzed with an electrochemical workstation (CHI 6005E, Chenhua Instruments, China) in a quartz cell equipped with a standard three-electrode system. Each sample was coated on a titanium electrode and employed as the working electrode. Meanwhile, a Pt plate and saturated Ag/AgCl electrode were employed as the counter and reference electrode respectively. 0.003 mg of photocatalyst sample was distributed in C<sub>2</sub>H<sub>5</sub>OH and ultrasonicated for 10 mins prior to drop-casting the catalyst onto a 1 cm<sup>2</sup> fluorine-doped tin oxide (FTO) substrate. The film was subsequently oven-dried and the thin-film electrodes of CN, CQD/CN and 1-BCQD/CN were obtained. A 1.0 M Na<sub>2</sub>SO<sub>4</sub> was employed as the electrolyte. The evaluation of transient photocurrent response was carried out with the light being switched on and off by applying a bias of 0.35 V. The electrochemical impedance spectra (EIS) were evaluated over a frequency of 0.1–105 Hz and applied potential of 0.35 V vs. Ag/AgCl with an alternating current (AC) perturbation signal of 0.01 V under the irradiation of visible light ( $\lambda > 400$  nm). The Mott-Schottky plot of photocatalyst samples were obtained over a potential range of -1.0 to 1.0 V vs. Ag/AgCl.

## 2.6 Free radical scavenging tests

To investigate the photocatalytic mechanisms underlying BCQD/CN nanocomposites, a series of scavenging tests were conducted. 2-propanol (IPA), triethanolamine (TEOA) and p-benzoquinone (BZQ) were utilized to capture hydroxyl ( $\bullet$ OH), holes ( $h^+$ ) and superoxide anion ( $\bullet$ O<sub>2</sub><sup>-</sup>) radicals respectively. The concentrations of IPA and TEOA used in the scavenging tests was fixed at 1.2 vol %; while 0.6 vol % of BZQ was employed. The experimental setup for the scavenging analysis was identical to the procedure of photocatalytic activity evaluation as presented in Sect. 2.4.

## Results And Discussion

### 3.1 Characterization of CN, CQD/CN and 1-BCQD/CN

The surface structure and morphology of CN, CQD/CN and 1-BCQD/CN were analyzed using FESEM and TEM. The successful fabrication of an n/n-type g-C<sub>3</sub>N<sub>4</sub> homojunction (CN) was reported in our previous work (Phang et al., 2020a). As shown in Fig. 2(a), the FESEM image of CN features two-dimensional (2D) nanosheets with wide lateral dimensions. The formation of macro-scale g-C<sub>3</sub>N<sub>4</sub> was due to the stacking of 2D polymer molecules while the lamellar structure of g-C<sub>3</sub>N<sub>4</sub> was eventually produced as the planar structure of the molecules undergone distortion. Such distortion was reported to be a result of the enlarged space between g-C<sub>3</sub>N<sub>4</sub> polymer molecules developed during the release of ammonia gas during the calcination step (Song et al., 2020). In addition, the platelet-like structures were also observed to be highly porous with large spatial networks. Figure 2(b) and 2(c) illustrate the FESEM images of CQD/CN and 1-BCQD/CN. From the microscopy images, it is evident that the 2D nanosheet framework of g-C<sub>3</sub>N<sub>4</sub> was generally well-retained. This indicated that the introduction of CQDs and BCQDs had no substantial effects on the surface morphology of g-C<sub>3</sub>N<sub>4</sub>, which was consistent with previously reported studies (Liu et al., 2020; Seng et al., 2020).

EDX analysis was also conducted to investigate the elemental composition of each nanocomposite sample. Figure 2(d) presents the EDX spectra of CN, CQD/CN and 1-BCQD/CN, respectively. It can be observed that both CN and CQD/CN contained C, N and O elements while 1-BCQD/CN showed the presence of an additional B peak, which validated the successful doping of B onto pristine CQDs. The presence of C in the EDX spectra could be due to the amorphous carbon of g-C<sub>3</sub>N<sub>4</sub> nanosheets and co-catalyst CQDs. Meanwhile, the existence of N in the spectra could be ascribed to the construction of g-C<sub>3</sub>N<sub>4</sub> using heptazine (C<sub>6</sub>H<sub>3</sub>N<sub>7</sub>) as the fundamental building block of the graphitic carbon framework. Finally, the minor composition of O could be due to the formation of carboxyl groups (–COOH) during the synthesis of BCQDs as well as possible adsorption of water molecules on the photocatalyst surface.

Figure 3(a)-(c) present the TEM images of CN, CQD/CN and 1-BCQD/CN. Similar to the FESEM image, the TEM image of CN depicted in Fig. 3(a) features a highly porous 2D planar sheet with pores of estimated diameters ranging from 22–39 nm. Upon the incorporation of CQD and BCQD, no distinguishable changes were observed with regards to the surface morphology and structure of g-C<sub>3</sub>N<sub>4</sub>. The TEM images of CQD/CN and 1-BCQD/CN are depicted in Fig. 3(b) and (c) respectively. Monodispersed quasi-spherical dark spots with an average diameter range of 6.076 and 6.024 nm (see Fig. 3(d)) were observed on the CN sheets for CQD and 1-BCQD respectively. This indicated the successful formation of CQDs and BCQDs on the surface CN. The co-existence of BCQDs and CN with such close contact between them reaffirmed the successful preparation of the heterostructure nanocomposites. This unique 0D/2D layout is perceived to be beneficial for the effective transfer of photogenerated charge carriers, which will in turn lead to a reduction in electron-hole recombination rate.

The crystalline framework of CN, CQD/CN and 1-BCQD/CN were analyzed with XRD, a non-destructive test method for the identification of plane spacing and crystal structure based on monochromatic beam of X-rays. Figure 4(a) presents the XRD patterns of CN, CQD/CN and 1-BCQD/CN. Two distinctive diffraction peaks were displayed by all the as-prepared photocatalytic samples, which validated the

construction of stacked graphitic layers of g-C<sub>3</sub>N<sub>4</sub> (JCPDS, No. 87-1526) (Ran et al., 2019; Orooji et al., 2020). The peak observed at a lower diffraction angle of 13.4° (d = 0.67 nm) corresponded to the (100) plane associated with the in-plane structural packing motif of heptazine units (Tyborski et al., 2013). On the other hand, a more-apparent peak located at approximately 27.4° (d = 0.325 nm) could be indexed to the (002) plane, corresponding to the typical interplanar stacking layers of conjugated aromatic compounds (Elshafie et al., 2020). It should be noted that all samples (CN, CQD/CN and 1-BCQD/CN) exhibited identical XRD trends. This indicated that the hybridization of CN with CQD or BCQD did not alter its fundamental crystalline layout, which was consistent with the microscopy images in Figs. 2 and 3. Interestingly, the characteristic peaks associated with CQD or BCQD were not observed in the XRD profiles. This may ascribe to the low quantity of quantum dots employed in the nanocomposite samples. Another possible reason for this observation could be the overshadowing of amorphous CQD by highly crystalline g-C<sub>3</sub>N<sub>4</sub> polymers. Similar findings were also reported in several published work, where the hybridization of CQDs with different semiconducting materials (e.g. CQD/Fe<sub>2</sub>O<sub>3</sub> and NCQD/TiO<sub>2</sub>) were studied (Zhang et al., 2011; Martins et al., 2016). Figure 4(b) shows the magnified XRD profiles of CN, CQD/CN and 1-BCQD/CN between 26–29°, where the (002) peaks were respectively located at 27.34°, 27.32° and 27.37° respectively. Generally, a slight right-shift in the XRD peak is an implication of narrower interlayer and intralayer distances (Zhang et al., 2018). The full width at half maximum (FWHM) of the (002) peak was sequenced in an increasing order of CN, CQD/CN and 1-BCQD/CN, which indicated that 1-BCQD/CN possessed the greatest crystallite size in comparison with that of CN and CQD/CN.

The molecular structure and chemical composition of CN, CQD/CN and 1-BCQD/CN were also analyzed via FTIR as shown in Fig. 4(c). For CQD/CN and 1-BCQD/CN nanocomposites, the broad band at 3260 cm<sup>-1</sup> was ascribed to the stretching of -OH groups with the presence of CQD and BCQD (Zhang et al., 2017b). Apart from that, there were no observable changes to the transmittance peaks of the samples. This once again affirmed the well-preserved chemical framework of CN with the coupling of CQD and BCQD. The sharp peaks located in the range of 1200–1650 cm<sup>-1</sup> could be attributed to the stretching modes of -C-N heterocycles, displaying peaks located at 1646 cm<sup>-1</sup>, 1578 cm<sup>-1</sup>, 1411 cm<sup>-1</sup>, 1329 cm<sup>-1</sup>, and 1235 cm<sup>-1</sup> (Kumru et al., 2019; Seng et al., 2020). On the other hand, the peak at 1081 cm<sup>-1</sup> could be associated to the oxygenated functional group C-O (Wang et al., 2017b). The typical breathing mode of tri-s-triazine unit of g-C<sub>3</sub>N<sub>4</sub> homojunction was represented by the intense peak at 808 cm<sup>-1</sup> (Zhang et al., 2020a).

To gain a deeper understanding of the chemical interactions, XPS analysis was carried out to identify the elemental composition and bonding on the surface of the photocatalysts. As shown in Fig. 5(a), the survey spectra of CN, CQD/CN and 1-BCQD/CN show that the samples were primarily composed of C, N and O. The atomic concentrations and weight percentages of each element are summarized in Fig. 5(e). Intriguingly, the B element was not detected in the 1-BCQD/CN sample, which could be due to the low quantity of dopant used on the hybrid nanocomposite. Nevertheless, the successful integration of the B dopant was verified through EDX analysis as discussed earlier (see Fig. 2(f)). Figure 5(b) presents the

deconvoluted C 1s spectra of 1-BCQD/CN, where four prominent peaks at 288.85, 288.15, 285.70 and 284.72 eV were observed. These peaks corresponded to the C-N-C bonds, sp<sup>2</sup>-hybridized atomic carbon in N-C = N of the aromatic systems, C-O/C = O and C-C/C = C coordination, respectively (Liu et al., 2011; Qiao et al., 2015; Tan et al., 2015; Qin and Zeng, 2017). Besides that, the N 1s core level spectrum as depicted in Fig. 5(c) displayed a dominant peak centered at 398.57 eV, which could be associated to the pyridine N atom of the s-triazine rings (Sun et al., 2015; Cao et al., 2018). The N peak at 399.64 eV could be attributed to the pyrrolic N atom as part of the  $\pi$ -bonding system while the peak at 400.95 eV was ascribable to the graphitic N atom bonded to three carbon atoms within the aromatic rings (Kundu et al., 2010; Qiao et al., 2015; Fontelles-Carceller et al., 2016). The O 1s spectra, as shown in Fig. 5(d) was deconvoluted to two fitted peaks: 533.09 eV and 531.71 eV, which corresponded to -OH and C-O/C = O bonds respectively. These represented the oxygenic components of the B-doped CQDs which was similarly reported in literature (Qin and Zeng, 2017; Kesarla et al., 2019).

The optical properties of the as-developed photocatalysts were studied using UV-Vis DRS. As presented in Fig. 6(a), the adsorption bands of CN, CQD/CN and 1-BCQD/CN were categorized under the violet-blue regime of the visible spectrum. As observed from Fig. 6(a), the samples presented similar optical absorbances with absorption edges of CN, CQD/CN and 1-BCQD/CN at *ca.* 460, 453 and 452 nm respectively. As the changes in the absorption edge of bulk and CQDs-based CN was relatively insignificant, it is reasonable to infer that CQDs primarily served as electron transfer conduits to enhance the transportation of photoinduced charge carriers (Seng et al., 2020). The measurements obtained were similar to the typical optical absorption of g-C<sub>3</sub>N<sub>4</sub> published in the previous studies (Liu et al., 2011; Yan et al., 2020).

The optical band gap energy ( $E_g$ ) of a semiconductor is defined as the energy difference between the highest occupied state in the VB and the lowest unoccupied state in the CB. The  $E_g$  can be determined via the construction of a Tauc plot i.e., a graph of  $[F(R) \cdot h\nu]^n$  vs. photon energy ( $h\nu$ ) (Viezbicke et al., 2015). The absorption coefficient, Planck constant and optical frequency are denoted as  $F(R)$ ,  $h$  and  $\nu$  respectively whereas the value of exponent  $n$  depends on the transition nature of the material (Xu and Gao, 2012; Kumar et al., 2017). As presented in Fig. 6(b), the  $E_g$  values of CN, CQD/CN and 1-BCQD/CN were approximately 2.70, 2.76 and 2.78 eV respectively. The widening of  $E_g$  upon CQD or BCQD doping could be ascribed to the quantum size effect as well as the presence of structural defects in the hybrid nanocomposites (Liu et al., 2007; Klubnuan et al., 2016).

## 3.2 Evaluation of photocatalytic activity

The photocatalytic activities of CN, CQD/CN and BCQD/CN (with varying mass loadings of the B dopant) were assessed via the photodegradation of organic dye RhB. Prior to light illumination, the suspension of photocatalyst and dye solution was stirred for 30 min without light to establish an adsorption-desorption equilibrium. The almost-complete saturation at the solid-liquid interface minimizes the effect of physical interaction on the changes in RhB concentration as photocatalytic reaction occurs (Zhang et al., 2016a). The photocatalytic experiments were carried out under the irradiation of an 18 W LED light for a total

duration of 4 hrs. The primary objectives of this study are: (i) to analyze the effect of incorporating B-dopant on CQDs-decorated n/n junctioned g-C<sub>3</sub>N<sub>4</sub>; and (ii) to investigate the optimum mass loading of B on the hybrid sample. Control experiments were also conducted following the procedures outlined in Sect. 2.4, but without (i) the photocatalyst sample; and (ii) light source (see Supplementary Information – Sect. 1.0). In both conditions, no significant discoloration of RhB was observed, which confirmed the indispensable roles of the photocatalyst and excitation source for the photodegradation process. Figure 7(a) shows the graph of  $\ln(C_0/C)$  against irradiation time of each photocatalyst sample for the evaluation of the  $k$  value according to the Langmuir-Hinshelwood model. The best-fitted lines signified the linear relationship between  $\ln(C_0/C)$  and irradiation time, thereby confirming that the photocatalytic degradation of RhB dye was in accord with the first-order kinetics.

Figure 7(b) depicts an overview of the photodegradation efficiencies and kinetic rate constants of CN, CQD/CN and BCQD/CN with varying mass loadings of B (0.5-BCQD/CN, 1-BCQD/CN, 2-BCQD/CN and 3-BCQD/CN). As observed, the photocatalytic performances were in the order of: 1-BCQD/CN > 2-BCQD/CN > 3-BCQD/CN > 0.5-BCQD/CN > CQD/CN > CN. In comparison to pure CN and CQD/CN, all B-modified CQD/CN photocatalysts displayed a pronounced improvement in photoactivities. The optimum 1-BCQD/CN sample achieved a remarkable 96.8% removal of RhB dye in 4 hrs under LED light illumination with an associated  $k$  value of  $1.39 \times 10^{-2} \text{ min}^{-1}$ . This translated to an improvement factor of 3.6 and 2.8 over pure CN and CQD/CN, which validated the significance of heteroatom B doping on CQDs for photocatalytic activity enhancement. The discoloration process of RhB in the presence of 1-BCQD/CN is shown in inset of Fig. 7(d). Interestingly, the color of the organic dye was observed to change progressively from its characteristic pink shade to orange and yellow, before turning colourless eventually.

As demonstrated in Fig. 7(b), the mass loading of B on CQD/CN did not impose prominent effects on the photodegradation efficiency of the hybrid material. However, its profound impact on the apparent rate constant was evident. Based on Fig. 7(b), the evaluated rate constant demonstrated an appreciable surge from  $1.09 \times 10^{-2} \text{ min}^{-1}$  (0.5-BCQD/CN) to  $1.46 \times 10^{-2} \text{ min}^{-1}$  (1-BCQD/CN). This observation highlighted the significance of precise mass loading of the B-dopant on CQD/CN in terms of expediting interfacial charge transfer and hindering electron-hole recombination. Figure 7(c) shows the absorbance trend exhibited by the RhB solution catalyzed over 1-BCQD/CN sample under visible light irradiation. For a RhB dye, the characteristic peak of the absorbance curve was noted at a wavelength of 554 nm prior to photodegradation. Apart from the gradual decrease in absorbance intensity with time, the peaks shifted gradually towards the blue region (left) of the visible spectrum as the illumination time lengthened. This was in congruent with the reported studies on the photodegradation of RhB catalyzed by g-C<sub>3</sub>N<sub>4</sub>/g-C<sub>3</sub>N<sub>4</sub> homojunction systems, Ag<sub>3</sub>PO<sub>4</sub> nanoparticles and Ag<sub>3</sub>VO<sub>4</sub>/β-Ag<sub>3</sub>VO<sub>4</sub> nanocomposites (Gao et al., 2017; Xu et al., 2017; Phang et al., 2020a). Besides, the left-shifted peaks signified the generation of de-ethylated intermediates as the chromophores and aromatic rings of the RhB dye undergone deconstruction (Li et al., 2008; Chiu et al., 2019)

### 3.3 Photoelectrochemical and PL analysis

To further study the charge migration behavior and separation of photo-generated electron-hole pairs across the interface of BCQD/CN photocatalyst, transient photocurrent response and Mott-Schottky plots were also constructed. As presented in Fig. 8(a), the transient photocurrent measured were plotted with respect to time for CN, CQ/CN and 1-BCQD/CN with alternate cycles of on-off visible light irradiation to study their photoelectronic properties. The electric current generated by the photo-excited charge carriers were measured via transient photocurrent as the visible light pulse was turned on and decayed promptly with the light shut off (Xiang et al., 2011; Phang et al., 2020a). It is observed that there was a significant improvement in the transient photocurrent response exhibited by 1-BCQD/CN. The relatively high current density of 1-BCQD/CN is an implication of the boosted effectiveness in electron-hole pairs separation which may be ascribed to the presence of BCQDs. The doping of BCQDs on CN played a significant role as the channels for electron transport (as discussed previously in Sect. 3.2) and this inference was further supported by the generally low Fermi level of CQDs (-0.3 eV) relative to that of CN (-0.61 eV) (Tian et al., 2017; Wang et al., 2017a). Thus, the photoinduced electrons were prompted to shuttle from CN to BCQDs, in which the BCQDs served as electron traps, to effectively retard the recombination of electron-hole pairs (Wang et al., 2018; Di et al., 2020).

Moreover, Mott-Schottky analysis were performed as an effort to analyze the interrelation between applied potential and capacitance space charge region. Figure 8(b) presents the Mott-Schottky plots of the photocatalyst samples and the flat band potential ( $E_{fb}$ ) was evaluated via the extrapolation of tangent lines at the x-axis intercept whereby  $C^{-2} = 0$ . From the Mott-Schottky plot, the  $E_{fb}$  of CN, CQD/CN and 1-BCQD/CN were determined as -0.70, -0.74 and - 0.77 V vs. Ag/AgCl respectively. The  $E_{fb}$  was marginally lowered with the incorporation of CQD and BCQD, indicating a depletion in photo-generated holes on the surface of the hybrid photocatalysts (Rangaraju et al., 2009; Liu et al., 2014). On top of that, Mott-Schottky plots of the samples displayed positive slopes which is the typical characteristic of an n-type semiconductor (Guan et al., 2020). Hence, this verified the successful construction of photocatalytic nanocomposites featuring n/n homojunction via coupling of g-C<sub>3</sub>N<sub>4</sub> derived from urea and thiourea. The measured flat band potentials are with respect to NHE) using the conversion equation as expressed in Eq. (3) whereby pH value was approximately 7.0 and  $E_{AgCl} = 0.197$  V at ambient temperature (Babu et al., 2018; Li et al., 2020a):

$$E_{fb}(vs.NHE) = E_{fb}(vs.Ag/AgCl) + E_{(AgCl)} + 0.059pH \quad (3)$$

Upon conversion, the  $E_{fb}$  (vs. NHE) of CN, CQD/CN and 1-BCQD/CN were evaluated as -0.09, -0.13 and - 0.16 V respectively. It is well-entrenched that the  $E_{cb}$  of an n-type semiconductor is generally 0.1–0.3 V more negative than its  $E_{fb}$ , as governed by the electron effective mass and carrier concentration (Tian et al., 2015). In this case, the difference in voltage between  $E_{fb}$  and  $E_{cb}$  was set at 0.3 V. Therefore, the  $E_{cb}$  were calculated as -0.39, -0.43 and - 0.46 V for CN, CQD/CN and 1-BCQD/CN respectively. Subsequently, the valence band potential,  $E_{vb}$  were evaluated according to the equation as follows:

$$E_{vb} = E_{cb} + E_g \quad (4)$$

The  $E_{vb}$  of CN, CQD/CN and 1-BCQD/CN were obtained as 2.31, 2.33 and 2.32 V respectively.

The PL spectra exhibited by CN, CQD/CN and 1-BCQD/CN were also presented in Fig. 8(c). Hitherto, the governing factor of PL mechanism has yet to be thoroughly elucidated and remains highly debatable as there are multiple argumentations regarding this subject matter. The proposed concepts include quantum confinement effect, functional groups, structural defect, surface passivation and functionalization, etc (Wang et al., 2014; Choi et al., 2016; Das et al., 2017). Nonetheless, it has been widely perceived that the intensity of PL emission is closely associated with the recombination of photo-excited charge carriers. Thus, PL spectra are commonly utilized to interpret the migration behavior, separation and transfer mechanism of electron-hole pairs (Zhu et al., 2019). Based on Fig. 8(c), the PL emission spectra of CN, CQD/CN and 1-BCQD/CN featured a prominent luminescence peak ranging from 420–520 nm. As it is well known, intense fluorescence (FL) emission implies a high rate of electron-hole recombination, whereby photogenerated holes from the lower energy states and electrons from the higher energy states recombine to release energy in the form of light (Wang et al., 2020). It is observed from Fig. 8(c) that CN exhibited the strongest PL emission spectra. On the contrary, relatively low PL emission peaks were demonstrated by CQD/CN and 1-BCQD/CN, reflecting the suppressed electron-hole recombination in the presence of pristine or B-doped CQDs. This also reaffirmed the role of CQDs in the hybridized photocatalytic nanocomposites as an electron transport conduit, considerably boosting the effectiveness of charge carrier transport and separation. Fundamentally, a low charge carriers recombination rate is highly beneficial towards the photocatalytic efficiency of a semiconductor nanomaterial.

### **3.7 Free radical scavenging test and plausible photocatalytic charge transfer mechanism**

A series of scavenging tests were performed to identify the role of each reactive species in the photocatalytic mineralization of RhB and to propose a plausible photocatalytic mechanism over BCQD/CN. The declined photocatalytic performance in the presence of each scavenger implied the importance of the associated reactive species. The scavenging chemicals, TEOA, BZQ and IPA were applied to capture the relevant reactive species,  $h^+$ ,  $\bullet O_2^-$  and  $\bullet OH$  respectively. The changes in concentration of RhB and degradation efficiency of BCQD-CN are summarized in Fig. 9(a). As observed in Fig. 9(b), it is evident that there was a drastic decrease in photoactivity upon the addition of TEOA (scavenger of  $h^+$ ), indicating that  $h^+$  species were indispensable for RhB photodegradation. Precisely,  $h^+$  reactive species held a crucial role in the generation of radicals including  $\bullet OH$  and  $OH^-$ , which actively took part in the mineralization of RhB ions ( $RhB^+$ ) into photodegraded products. In the absence of  $h^+$  species, the generation of  $\bullet OH$  radicals is not viable as the oxidation potential of water ( $H_2O/\bullet OH = +2.73$  eV) is more positive than the VB potential of the photocatalyst sample (Wang et al., 2017a). Nevertheless,  $\bullet OH$  radicals could also be generated via a different pathway whereby the reduction of elementary oxygen leads to the formation of  $\bullet O_2^-$  species, which are then further reduced to  $\bullet OH$  radicals through multiple-electron reduction reactions. In addition, the VB potential of BCQD/CN was more positive than the standard redox potential of waterborne hydroxyl radicals ( $\bullet OH/OH^- = +1.99$  eV), rendering the oxidation of  $OH^-$  feasible (Wu et al., 2015). In short, these reactive species are crucial in the degradation and mineralization of  $RhB^+$  under light irradiation.

Based on the scavenging test, a plausible step-by-step charge transfer mechanism for RhB photodegradation is presented in Fig. 10. The entire photo-reaction is initiated by the irradiation of visible light, where the electrons from VB are excited and directed towards CB. Upon the departure of electrons, holes are generated at the VB concurrently. Due to the difference in CB and VB levels of g-C<sub>3</sub>N<sub>4</sub> homojunction derived from urea and thiourea, the photo-generated electrons and holes are separated more effectively in comparison to the charge transfer within a pristine g-C<sub>3</sub>N<sub>4</sub> (Liu et al., 2018).

Specifically, the flow of photogenerated electrons (e<sup>-</sup>) is directed from the higher CB level of thiourea to that of urea while majority of the photogenerated holes (h<sup>+</sup>) are prompted to flow from the lower VB level of urea to that of thiourea. The opposite direction in flow of charge carriers minimizes the recombination possibility for electrons and holes. Furthermore, the doping of CQDs with heteroatoms B enriched the presence of structural defects on the functionalized surface of BCQDs, effectively trapping more photo-excited charge carriers and hampered the recombination of electrons and holes (Peng et al., 2020). Consequently, the photoinduced electrons from VB of CN are readily transferred to the BCQDs due to their lower energy levels (Wang et al., 2017a). The electrons are also captured and accumulated in the BCQDs attributed to their excellent conductivity and large capacity for electron storage (Ong et al., 2017). The electrons accumulated in the BCQDs and remnant of electrons in CN are primarily responsible for the reduction of O<sub>2</sub> to generate superoxide anion radicals (•O<sub>2</sub><sup>-</sup>). The reduction process is feasible as the CB levels of the nanocomposite is more negative than the redox potential of O<sub>2</sub>/•O<sub>2</sub><sup>-</sup> at -0.16 V (Krumova and Cosa, 2016). The •O<sub>2</sub><sup>-</sup> radicals are indispensable for the mineralization of RhB dye as evidenced by the scavenging test. On the other hand, the photoinduced holes in VB are gradually transported to the surface and participate in the oxidation process of hydroxyl species into hydroxyl radicals (•OH) as the VB level of BCQD/CN is more positive as compared to the redox potential of OH<sup>-</sup>/•OH at + 1.89 V (Armstrong et al., 2015). It is also worth mentioning that the change in redox potential ability upon hybridization is negligible as ratiocinated from the evaluated VB and CB energy levels of pristine CN, CQD- and BCQD-based CN. Therefore, it is reasonable to deduce that the BCQD and/or CQD mainly acted as channels to facilitate electron transport and storage for the photocatalytic enhancement. Another factor that should be taken into consideration for RhB photodegradation is the challenge of possible colloidal instability, competition over active sites and susceptible hole scavenging posed by the inorganic chloride anions (Cl<sup>-</sup>) (Chong et al., 2010). Nonetheless, the presence of π-π interactions on the exterior of the nanocomposite photocatalyst enhanced the adsorption of organic pollutants, resulting in a boosted photocatalytic efficiency. Ultimately, the mineralization process of RhB pollutants was expedited by reactive species including •OH, •O<sub>2</sub><sup>-</sup> and h<sup>+</sup> in the formation of photo-degraded products.

### 3.8 Recyclability test

In addition to the initial photocatalytic performance, the reusability of photocatalysts is also critical for practical and long-term applications. For the evaluation of its photo-stability, the optimal sample, 1-BCQD/CN was assessed and recycled for 3 consecutive cycles under identical conditions. The photocatalyst sample was separated from the dye solution via vacuum filtration and washed copiously with distilled water prior to oven-drying for the subsequent cycle. To account for the weight loss in the

recovered photocatalyst sample, the amount lost was compensated by a decreased volume of dye solution following a fixed ratio of 0.15 g photocatalyst to 100 mL RhB solution (10 mg/L). The recyclability test of 1-BCQD/CN is presented in Fig. 11(a). It is apparent that the photoactivity of 1-BCQD/CN was successfully retained even after 3 successive cycles without any observable regression in its photocatalytic performance. Precisely, the 1-BCQD/CN photocatalyst sample maintained 98.6 % of its original activity after 3 consecutive runs. Furthermore, there were no significant changes to the molecular structure and chemical composition of the recycled 1-BCQD/CN with reference to its fresh counterpart as evidenced by their respective FTIR spectra presented in Fig. 11(b). This suggests that 1-BCQD/CN is superior in term of its stability and durability, which are highly advantageous from the economic and sustainability perspectives for probable industrial applications in the future.

## Conclusion

In summary, novel metal-free composite photocatalysts (BCQD/CN) were successfully fabricated by hybridizing B-doped CQDs and n/n-type  $g\text{-C}_3\text{N}_4$  homojunction derived from equal proportion of urea and thiourea. Different amounts of B dopant were applied to determine the appropriate dosage in optimizing the photocatalytic efficiency of BCQD/CN nanocomposite. The successful incorporation of BCQDs and CQDs into  $g\text{-C}_3\text{N}_4/g\text{-C}_3\text{N}_4$  homojunction was verified via a series of characterization analyses including FESEM, TEM, EDX, XRD, FTIR and XPS. These tests have successfully proven the co-existence of BCQDs and CN which were bonded together securely as distinguished through the changes in their surface morphologies, crystalline structures, chemical compositions, etc. PL and UV-Vis DRS were also carried out to study the optical properties of the as-synthesized photocatalyst samples by evaluating their band gap structures and charge transfer behaviours. The optimized photocatalytic nanocomposite, 1-BCQD/CN with a mass ratio of boric acid to citric acid at 1:3 displayed a marginally higher photocatalytic performance relative to other BCQD/CN samples with a RhB photodegradation efficiency 31 % and 40 % higher than that of CQD/CN and CN respectively. There are several contributing factors to the boosted photoactivity of BCQD/CN nanocomposites, including the synergistic effects of (1) promoted electron charge transport from CN to BCQDs, (2) suppressed recombination rate of electron-hole pairs and (3) improved charge density in facilitating charge migration. The photoactivity evaluation of RhB degradation was conducted under the illumination of an 18W LED light. The remarkable photo-efficiency displayed by BCQD/CN toward RhB degradation despite the relatively low-powered with a relatively low-powered light source highlights the various benefits from the environmental and economic perspectives. This offers an optimistic outlook to the possible industrial-scale operation for wastewater treatment by means of photocatalysis in the near future. On top of that, the durability of 1-BCQD/CN was also validated by subjecting it to 3 consecutive cycles of RhB photodegradation under identical conditions, where no observable regression in photoactivity was observed. A plausible photocatalytic mechanism for RhB degradation in the presence of BCQD/CN was also proposed by identifying the roles of specific reactive species through a series of scavenging tests. On the whole, this research work is expected to provoke more pioneering research ideas in the development of photocatalytic semiconductors as a robust

approach to various pressing global challenges, particularly the environmental- and energy-related matters.

## **Declarations**

### **Ethics approval and consent to participate**

Not applicable

### **Consent for publication**

Not applicable

### **Availability of data and materials**

All data generated or analyzed during this study are included in this published article [and its supplementary information files].

### **Competing interests**

The authors declare that they have no competing interests.

### **Funding**

This work was funded by the Ministry of Higher Education (MOHE) Malaysia under the Fundamental-Research Grant Scheme (FRGS) (Ref no: FRGS/1/2018/TK02/HWUM/03/2).

### **Authors' contributions**

All authors contributed to the study conception and design. Material preparation, data collection and analysis were performed by SP and JL. The research work was supervised by VW, LT and SC. The first draft of the manuscript was written by SP and all authors commented on previous versions of the manuscript. All authors read and approved the final manuscript.

### **Acknowledgements**

This work was funded by the Ministry of Higher Education (MOHE) Malaysia under the Fundamental-Research Grant Scheme (FRGS) (Ref no: FRGS/1/2018/TK02/HWUM/03/2).

## References

1. An H-R, Park SY, Kim H, Lee CY, Choi S, Lee SC, Seo S, Park EC, Oh Y-K, Song C-G, Won J, Kim YJ, Lee J, Lee HU, Lee Y-C (2016) Advanced nanoporous TiO<sub>2</sub> photocatalysts by hydrogen plasma for efficient solar-light photocatalytic application. *Sci Rep* 6(1):29683
2. Armstrong DA, Huie RE, Koppenol WH, Lyman SV, Merényi G, Neta P, Ruscic B, Stanbury DM, Steenken S, Wardman P (2015) Standard electrode potentials involving radicals in aqueous solution: inorganic radicals (IUPAC Technical Report). *Pure and Applied Chemistry*, 87(11–12): 1139–1150
3. Babu P, Mohanty S, Naik B, Parida K (2018) Synergistic Effects of Boron and Sulfur Co-doping into Graphitic Carbon Nitride Framework for Enhanced Photocatalytic Activity in Visible Light Driven Hydrogen Generation. *ACS Applied Energy Materials* 1(11):5936–5947
4. Bhati A, Anand SR, Saini D, Sonkar SK (2019) Sunlight-induced photoreduction of Cr (VI) to Cr (III) in wastewater by nitrogen-phosphorus-doped carbon dots. *npj Clean Water* 2(1):1–9
5. Cao S, Shen B, Tong T, Fu J, Yu J (2018) 2D/2D heterojunction of ultrathin MXene/Bi<sub>2</sub>WO<sub>6</sub> nanosheets for improved photocatalytic CO<sub>2</sub> reduction. *Adv Func Mater* 28(21):1800136
6. Che H, Liu L, Che G, Dong H, Liu C, Li C (2019) Control of energy band, layer structure and vacancy defect of graphitic carbon nitride by intercalated hydrogen bond effect of NO<sub>3</sub> – toward improving photocatalytic performance. *Chem Eng J* 357:209–219
7. Chen P-W, Li K, Yu Y-X, Zhang W-D (2017) Cobalt-doped graphitic carbon nitride photocatalysts with high activity for hydrogen evolution. *Appl Surf Sci* 392:608–615
8. Chiu Y-H, Chang T-FM, Chen C-Y, Sone M, Hsu Y-J (2019) Mechanistic insights into photodegradation of organic dyes using heterostructure photocatalysts. *Catalysts* 9(5):430
9. Choi Y, Kang B, Lee J, Kim S, Kim GT, Kang H, Lee BR, Kim H, Shim S-H, Lee G, Kwon O-H, Kim B-S (2016) Integrative Approach toward Uncovering the Origin of Photoluminescence in Dual Heteroatom-Doped Carbon Nanodots. *Chem Mater* 28(19):6840–6847
10. Chong MN, Jin B, Chow CWK, Saint C (2010) Recent developments in photocatalytic water treatment technology: A review. *Water Res* 44(10):2997–3027
11. Cushing SK, Meng F, Zhang J, Ding B, Chen CK, Chen C-J, Liu R-S, Bristow AD, Bright J, Zheng P, Wu N (2017) Effects of Defects on Photocatalytic Activity of Hydrogen-Treated Titanium Oxide Nanobelts. *ACS Catalysis* 7(3):1742–1748
12. Das A, Gude V, Roy D, Chatterjee T, De CK, Mandal PK (2017) On the Molecular Origin of Photoluminescence of Nonblinking Carbon Dot. *J Phys Chem C* 121(17):9634–9641
13. Di G, Zhu Z, Dai Q, Zhang H, Shen X, Qiu Y, Huang Y, Yu J, Yin D, Küppers S (2020) Wavelength-dependent effects of carbon quantum dots on the photocatalytic activity of g-C<sub>3</sub>N<sub>4</sub> enabled by LEDs. *Chem Eng J* 379:122296
14. Elshafie M, Younis SA, Serp P, Gad E a M (2020) Preparation characterization and non-isothermal decomposition kinetics of different carbon nitride sheets. *Egyptian Journal of Petroleum*, 29(1): 21–29

15. Fontelles-Carceller O, Muñoz-Batista MJ, Fernández-García M, Kubacka A (2016) Interface Effects in Sunlight-Driven Ag/g-C<sub>3</sub>N<sub>4</sub> Composite Catalysts: Study of the Toluene Photodegradation Quantum Efficiency. *ACS Appl Mater Interfaces* 8(4):2617–2627
16. Gao L, Li Z, Liu J (2017) Facile synthesis of Ag<sub>3</sub>VO<sub>4</sub>/β-AgVO<sub>3</sub> nanowires with efficient visible-light photocatalytic activity. *RSC Advances* 7(44):27515–27521
17. Guan M, Wang C, Li S, Du H, Yuan Y (2020) Understanding the Enhanced Electrocatalytic Hydrogen Evolution via Integrating Electrochemically Inactive g-C<sub>3</sub>N<sub>4</sub>: The Effect of Interfacial Engineering. *ACS Sustainable Chemistry Engineering* 8(27):10313–10320
18. Guo Y, Cao F, Li Y (2018) Solid phase synthesis of nitrogen and phosphor co-doped carbon quantum dots for sensing Fe<sup>3+</sup> and the enhanced photocatalytic degradation of dyes. *Sens Actuators B* 255:1105–1111
19. Hasija V, Raizada P, Sudhaik A, Sharma K, Kumar A, Singh P, Jonnalagadda SB, Thakur VK (2019) Recent advances in noble metal free doped graphitic carbon nitride based nanohybrids for photocatalysis of organic contaminants in water: A review. *Applied Materials Today* 15:494–524
20. Hu J, Chen D, Mo Z, Li N, Xu Q, Li H, He J, Xu H, Lu J (2019) Z-Scheme 2D/2D Heterojunction of Black Phosphorus/Monolayer Bi<sub>2</sub>WO<sub>6</sub> Nanosheets with Enhanced Photocatalytic Activities. *Angew Chem Int Ed* 58(7):2073–2077
21. Jeevitha G, Abhinayaa R, Mangalaraj D, Ponpandian N (2018) Tungsten oxide-graphene oxide (WO<sub>3</sub>-GO) nanocomposite as an efficient photocatalyst, antibacterial and anticancer agent. *J Phys Chem Solids* 116:137–147
22. Jiao X, Zheng K, Hu Z, Sun Y, Xie Y (2020) Broad-Spectral-Response Photocatalysts for CO<sub>2</sub> Reduction. *ACS Central Science* 6(5):653–660
23. Kesarla MK, Fuentes-Torres MO, Alcludia-Ramos MA, Ortiz-Chi F, Espinosa-González CG, Aleman M, Torres-Torres JG, Godavarthi S (2019) Synthesis of g-C<sub>3</sub>N<sub>4</sub>/N-doped CeO<sub>2</sub> composite for photocatalytic degradation of an herbicide. *Journal of Materials Research Technology* 8(2):1628–1635
24. Klubnuan S, Suwanboon S, Amornpitoksuk P (2016) Effects of optical band gap energy, band tail energy and particle shape on photocatalytic activities of different ZnO nanostructures prepared by a hydrothermal method. *Opt Mater* 53:134–141
25. Kooshki H, Sobhani-Nasab A, Eghbali-Arani M, Ahmadi F, Ameri V, Rahimi-Nasrabadi M (2019) Eco-friendly synthesis of PbTiO<sub>3</sub> nanoparticles and PbTiO<sub>3</sub>/carbon quantum dots binary nano-hybrids for enhanced photocatalytic performance under visible light. *Sep Purif Technol* 211:873–881
26. Krumova K, Cosa G (2016) Singlet Oxygen: Applications in Biosciences and Nanosciences, vol 1. The Royal Society of Chemistry, pp 1–21
27. Kumar S, Kumar A, Bahuguna A, Sharma V, Krishnan V (2017) Two-dimensional carbon-based nanocomposites for photocatalytic energy generation and environmental remediation applications. *Beilstein journal of nanotechnology* 8(1):1571–1600

28. Kumru B, Barrio J, Zhang J, Antonietti M, Shalom M, Schmidt BVKJ (2019) Robust Carbon Nitride-Based Thermoset Coatings for Surface Modification and Photochemistry. *ACS Appl Mater Interfaces* 11(9):9462–9469
29. Kundu S, Xia W, Busser W, Becker M, Schmidt DA, Havenith M, Muhler M (2010) The formation of nitrogen-containing functional groups on carbon nanotube surfaces: a quantitative XPS and TPD study. *Physical Chemistry Chemical Physics* 12(17):4351–4359
30. Li W, Ma Q, Wang X, Chu X-S, Wang F, Wang X-C, Wang C-Y (2020a) Enhanced photoresponse and fast charge transfer: three-dimensional macroporous g-C<sub>3</sub>N<sub>4</sub>/GO-TiO<sub>2</sub> nanostructure for hydrogen evolution. *Journal of Materials Chemistry A* 8(37):19533–19543
31. Li X, Ouyang S, Kikugawa N, Ye J (2008) Novel Ag<sub>2</sub>ZnGeO<sub>4</sub> photocatalyst for dye degradation under visible light irradiation. *Appl Catal A* 334(1):51–58
32. Li X, Zhao Z (2014) Facile ionic-liquid-assisted electrochemical synthesis of size-controlled carbon quantum dots by tuning applied voltages. *RSC Advances* 4(101):57615–57619
33. Li Y, Liu J, Wan X, Pan R, Bai B, Wang H, Cao X, Zhang J (2020b) Surface passivation enabled-structural engineering of I-III-VI<sub>2</sub> nanocrystal photocatalysts. *Journal of Materials Chemistry A* 8(19):9951–9962
34. Lim SY, Shen W, Gao Z (2015) Carbon quantum dots and their applications. *Chem Soc Rev* 44(1):362–381
35. Lin X, Liu C, Wang J, Yang S, Shi J, Hong Y (2019) Graphitic carbon nitride quantum dots and nitrogen-doped carbon quantum dots co-decorated with BiVO<sub>4</sub> microspheres: a ternary heterostructure photocatalyst for water purification. *Sep Purif Technol* 226:117–127
36. Liu J, Zhang T, Wang Z, Dawson G, Chen W (2011) Simple pyrolysis of urea into graphitic carbon nitride with recyclable adsorption and photocatalytic activity. *J Mater Chem* 21(38):14398–14401
37. Liu Q, Tian H, Dai Z, Sun H, Liu J, Ao Z, Wang S, Han C, Liu S (2020) Nitrogen-doped Carbon Nanospheres-Modified Graphitic Carbon Nitride with Outstanding Photocatalytic Activity. *Nano-Micro Letters* 12(1):24
38. Liu Y, Yu Y-X, Zhang W-D (2014) Photoelectrochemical study on charge transfer properties of nanostructured Fe<sub>2</sub>O<sub>3</sub> modified by g-C<sub>3</sub>N<sub>4</sub>. *Int J Hydrogen Energy* 39(17):9105–9113
39. Liu Z, Sun DD, Guo P, Leckie JO (2007) One-Step Fabrication and High Photocatalytic Activity of Porous TiO<sub>2</sub> Hollow Aggregates by Using a Low-Temperature Hydrothermal Method Without Templates. *Chemistry – A European Journal* 13(6):1851–1855
40. Liu Z, Wang G, Chen H-S, Yang P (2018) An amorphous/crystalline g-C<sub>3</sub>N<sub>4</sub> homojunction for visible light photocatalysis reactions with superior activity. *Chem Commun* 54(37):4720–4723
41. Luo PG, Sahu S, Yang S-T, Sonkar SK, Wang J, Wang H, Lecroy GE, Cao L, Sun Y-P (2013) Carbon “quantum” dots for optical bioimaging. *Journal of Materials Chemistry B* 1(16):2116–2127
42. Ma X, Lou Y, Chen J (2018) New UiO-66/CuxS Heterostructures: Surface Functionalization Synthesis and Their Application in Photocatalytic Degradation of RhB. *Bull Chem Soc Jpn* 91(4):515–522

43. Ma Y, Li X, Yang Z, Xu S, Zhang W, Su Y, Hu N, Lu W, Feng J, Zhang Y (2016) Morphology control and photocatalysis enhancement by in situ hybridization of cuprous oxide with nitrogen-doped carbon quantum dots. *Langmuir* 32(37):9418–9427
44. Ma Z, Ming H, Huang H, Liu Y, Kang Z (2012) One-step ultrasonic synthesis of fluorescent N-doped carbon dots from glucose and their visible-light sensitive photocatalytic ability. *New J Chem* 36(4):861–864
45. Martins NCT, Ângelo J, Girão AV, Trindade T, Andrade L, Mendes A (2016) N-doped carbon quantum dots/TiO<sub>2</sub> composite with improved photocatalytic activity. *Appl Catal B* 193:67–74
46. Mishra A, Mehta A, Basu S, Shetti NP, Reddy KR, Aminabhavi TM (2019) Graphitic carbon nitride (g-C<sub>3</sub>N<sub>4</sub>)-based metal-free photocatalysts for water splitting: a review. *Carbon* 149:693–721
47. Molaei MJ (2020) The optical properties and solar energy conversion applications of carbon quantum dots: A review. *Sol Energy* 196:549–566
48. Nassar MY, Abdelrahman EA (2017) Hydrothermal tuning of the morphology and crystallite size of zeolite nanostructures for simultaneous adsorption and photocatalytic degradation of methylene blue dye. *J Mol Liq* 242:364–374
49. Ong W-J, Putri LK, Tan Y-C, Tan L-L, Li N, Ng YH, Wen X, Chai S-P (2017) Unravelling charge carrier dynamics in protonated g-C<sub>3</sub>N<sub>4</sub> interfaced with carbon nanodots as co-catalysts toward enhanced photocatalytic CO<sub>2</sub> reduction: A combined experimental and first-principles DFT study. *Nano Research* 10(5):1673–1696
50. Organization WH (2019) Drinking Water: World Health Organization
51. Orooji Y, Ghanbari M, Amiri O, Salavati-Niasari M (2020) Facile fabrication of silver iodide/graphitic carbon nitride nanocomposites by notable photo-catalytic performance through sunlight and antimicrobial activity. *J Hazard Mater* 389:122079
52. Pan J, Zheng Z, Yang J, Wu Y, Lu F, Chen Y, Gao W (2017) A novel and sensitive fluorescence sensor for glutathione detection by controlling the surface passivation degree of carbon quantum dots. *Talanta* 166:1–7
53. Peng Z, Zhou Y, Ji C, Pardo J, Mintz KJ, Pandey RR, Chusuei CC, Graham RM, Yan G, Leblanc RM (2020) Facile synthesis of “boron-doped” carbon dots and their application in visible-light-driven photocatalytic degradation of organic dyes. *Nanomaterials* 10(8):1560
54. Phang SJ, Goh JM, Tan L-L, Lee WPC, Ong W-J, Chai S-P (2020a) Metal-free n/n-junctioned graphitic carbon nitride (g-C<sub>3</sub>N<sub>4</sub>): a study to elucidate its charge transfer mechanism and application for environmental remediation. *Environmental Science and Pollution Research*
55. Phang SJ, Tan L-L (2019) Recent advances in carbon quantum dots (CQDs)-based two dimensional materials for photocatalytic applications. *Catalysis Science & Technology*
56. Phang SJ, Wong V-L, Tan L-L, Chai S-P (2020b) Recent advances in homojunction-based photocatalysis for sustainable environmental remediation and clean energy generation. *Applied Materials Today* 20:100741

57. Qiao F, Wang J, Ai S, Li L (2015) As a new peroxidase mimetics: The synthesis of selenium doped graphitic carbon nitride nanosheets and applications on colorimetric detection of H<sub>2</sub>O<sub>2</sub> and xanthine. *Sens Actuators B* 216:418–427
58. Qin J, Zeng H (2017) Photocatalysts fabricated by depositing plasmonic Ag nanoparticles on carbon quantum dots/graphitic carbon nitride for broad spectrum photocatalytic hydrogen generation. *Appl Catal B* 209:161–173
59. Ran J, Ma TY, Gao G, Du X-W, Qiao SZ (2015) Porous P-doped graphitic carbon nitride nanosheets for synergistically enhanced visible-light photocatalytic H<sub>2</sub> production. *Energy Environ Sci* 8(12):3708–3717
60. Ran J, Pan T, Wu Y, Chu C, Cui P, Zhang P, Ai X, Fu C-F, Yang Z, Xu T (2019) Endowing g-C<sub>3</sub>N<sub>4</sub> Membranes with Superior Permeability and Stability by Using Acid Spacers. *Angew Chem Int Ed* 58(46):16463–16468
61. Rangaraju RR, Panday A, Raja KS, Misra M (2009) Nanostructured anodic iron oxide film as photoanode for water oxidation. *J Phys D: Appl Phys* 42(13):135303
62. Sahu RS, Shih Y-H, Chen W-L (2020) New insights of metal free 2D graphitic carbon nitride for photocatalytic degradation of bisphenol A. *Journal of Hazardous Materials*: 123509
63. Seng RX, Tan L-L, Lee WPC, Ong W-J, Chai S-P (2020) Nitrogen-doped carbon quantum dots-decorated 2D graphitic carbon nitride as a promising photocatalyst for environmental remediation: A study on the importance of hybridization approach. *J Environ Manage* 255:109936
64. Song B, Wang Q, Wang L, Lin J, Wei X, Murugadoss V, Wu S, Guo Z, Ding T, Wei S (2020) Carbon nitride nanoplatelet photocatalysts heterostructured with B-doped carbon nanodots for enhanced photodegradation of organic Pollutants. *J Colloid Interface Sci* 559:124–133
65. Sun Q, Lv K, Zhang Z, Li M, Li B (2015) Effect of contact interface between TiO<sub>2</sub> and g-C<sub>3</sub>N<sub>4</sub> on the photoreactivity of g-C<sub>3</sub>N<sub>4</sub>/TiO<sub>2</sub> photocatalyst:(0 0 1) vs (1 0 1) facets of TiO<sub>2</sub>. *Appl Catal B* 164:420–427
66. Tan L, Xu J, Zhang X, Hang Z, Jia Y, Wang S (2015) Synthesis of g-C<sub>3</sub>N<sub>4</sub>/CeO<sub>2</sub> nanocomposites with improved catalytic activity on the thermal decomposition of ammonium perchlorate. *Appl Surf Sci* 356:447–453
67. Tan S, Xing Z, Zhang J, Li Z, Wu X, Cui J, Kuang J, Yin J, Zhou W (2017) Meso-g-C<sub>3</sub>N<sub>4</sub>/g-C<sub>3</sub>N<sub>4</sub> nanosheets laminated homojunctions as efficient visible-light-driven photocatalysts. *Int J Hydrogen Energy* 42(41):25969–25979
68. Tian N, Huang H, Liu C, Dong F, Zhang T, Du X, Yu S, Zhang Y (2015) In situ co-pyrolysis fabrication of CeO<sub>2</sub>/gC<sub>3</sub>N<sub>4</sub>-n-n type heterojunction for synchronously promoting photo-induced oxidation and reduction properties. *Journal of Materials Chemistry A* 3(33):17120–17129
69. Tian N, Zhang Y, Li X, Xiao K, Du X, Dong F, Waterhouse GIN, Zhang T, Huang H (2017) Precursor-reforming protocol to 3D mesoporous g-C<sub>3</sub>N<sub>4</sub> established by ultrathin self-doped nanosheets for superior hydrogen evolution. *Nano Energy* 38:72–81

70. Tyborski T, Merschjann C, Orthmann S, Yang F, Lux-Steiner MC, Schedel-Niedrig T (2013) Crystal structure of polymeric carbon nitride and the determination of its process-temperature-induced modifications. *J Phys: Condens Matter* 25(39):395402
71. Viezbicke BD, Patel S, Davis BE, Birnie lii DP (2015) Evaluation of the Tauc method for optical absorption edge determination: ZnO thin films as a model system. *physica status solidi (b)* 252(8):1700–1710
72. Wang F, Chen P, Feng Y, Xie Z, Liu Y, Su Y, Zhang Q, Wang Y, Yao K, Lv W, Liu G (2017a) Facile synthesis of N-doped carbon dots/g-C<sub>3</sub>N<sub>4</sub> photocatalyst with enhanced visible-light photocatalytic activity for the degradation of indomethacin. *Appl Catal B* 207:103–113
73. Wang F, Wang Y, Feng Y, Zeng Y, Xie Z, Zhang Q, Su Y, Chen P, Liu Y, Yao K, Lv W, Liu G (2018) Novel ternary photocatalyst of single atom-dispersed silver and carbon quantum dots co-loaded with ultrathin g-C<sub>3</sub>N<sub>4</sub> for broad spectrum photocatalytic degradation of naproxen. *Appl Catal B* 221:510–520
74. Wang G, Zhang W, Li J, Dong X, Zhang X (2019a) Carbon quantum dots decorated BiVO<sub>4</sub> quantum tube with enhanced photocatalytic performance for efficient degradation of organic pollutants under visible and near-infrared light. *Journal of Materials Science* 54(8):6488–6499
75. Wang S, Kudrawiec R, Chi C, Zhang L, Zhang X, Ou X (2020) *Mid-infrared Optoelectronics*. Tournié, E. and Cerutti L (eds): Woodhead Publishing, pp 457–492
76. Wang W, Zeng Z, Zeng G, Zhang C, Xiao R, Zhou C, Xiong W, Yang Y, Lei L, Liu Y (2019b) Sulfur doped carbon quantum dots loaded hollow tubular g-C<sub>3</sub>N<sub>4</sub> as novel photocatalyst for destruction of *Escherichia coli* and tetracycline degradation under visible light. *Chem Eng J* 378:122132
77. Wang X, Cheng J, Yu H, Yu J (2017b) A facile hydrothermal synthesis of carbon dots modified g-C<sub>3</sub>N<sub>4</sub> for enhanced photocatalytic H<sub>2</sub>-evolution performance. *Dalton Trans* 46(19):6417–6424
78. Wang X, Wang F, Sang Y, Liu H (2017c) Full-Spectrum Solar-Light-Activated Photocatalysts for Light–Chemical Energy Conversion. *Advanced Energy Materials* 7(23):1700473
79. Wang Y, Kalytchuk S, Zhang Y, Shi H, Kershaw SV, Rogach AL (2014) Thickness-Dependent Full-Color Emission Tunability in a Flexible Carbon Dot Ionogel. *The Journal of Physical Chemistry Letters* 5(8):1412–1420
80. Weon S, He F, Choi W (2019) Status and challenges in photocatalytic nanotechnology for cleaning air polluted with volatile organic compounds: visible light utilization and catalyst deactivation. *Environmental Science: Nano* 6(11):3185–3214
81. Wu D, Wang B, Wang W, An T, Li G, Ng TW, Yip HY, Xiong C, Lee HK, Wong PK (2015) Visible-light-driven BiOBr nanosheets for highly facet-dependent photocatalytic inactivation of *Escherichia coli*. *Journal of Materials Chemistry A* 3(29):15148–15155
82. Xiang Q, Yu J, Jaroniec M (2011) Preparation and Enhanced Visible-Light Photocatalytic H<sub>2</sub>-Production Activity of Graphene/C<sub>3</sub>N<sub>4</sub> Composites. *J Phys Chem C* 115(15):7355–7363
83. Xu B, Wang X, Zhu C, Ran X, Li T, Guo L (2017) Probing the inhomogeneity and intermediates in the photosensitized degradation of rhodamine B by Ag<sub>3</sub>PO<sub>4</sub> nanoparticles from an ensemble to a single

- molecule approach. RSC Advances 7(65):40896–40904
84. Xu Y, Gao S-P (2012) Band gap of C<sub>3</sub>N<sub>4</sub> in the GW approximation. Int J Hydrogen Energy 37(15):11072–11080
  85. Yan B, Du C, Yang G (2020) Constructing Built-in Electric Field in Ultrathin Graphitic Carbon Nitride Nanosheets by N and O Codoping for Enhanced Photocatalytic Hydrogen Evolution Activity. Small 16(4):1905700
  86. Yang F, Lecroy GE, Wang P, Liang W, Chen J, Fernando KS, Bunker CE, Qian H, Sun Y-P (2016) Functionalization of Carbon Nanoparticles and Defunctionalization—Toward Structural and Mechanistic Elucidation of Carbon “Quantum” Dots. J Phys Chem C 120(44):25604–25611
  87. Yang J, Liang Y, Li K, Yang G, Wang K, Xu R, Xie X (2020) One-step synthesis of novel K<sup>+</sup> and cyano groups decorated triazine-/heptazine-based g-C<sub>3</sub>N<sub>4</sub> tubular homojunctions for boosting photocatalytic H<sub>2</sub> evolution. Appl Catal B 262:118252
  88. Ye B, Han X, Yan M, Zhang H, Xi F, Dong X, Liu J (2017) Fabrication of metal-free two dimensional/two dimensional homojunction photocatalyst using various carbon nitride nanosheets as building blocks. J Colloid Interface Sci 507:209–216
  89. Zhang G, Lan Z-A, Wang X (2016a) Conjugated Polymers: Catalysts for Photocatalytic Hydrogen Evolution. Angew Chem Int Ed 55(51):15712–15727
  90. Zhang H, Ming H, Lian S, Huang H, Li H, Zhang L, Liu Y, Kang Z, Lee S-T (2011) Fe<sub>2</sub>O<sub>3</sub>/carbon quantum dots complex photocatalysts and their enhanced photocatalytic activity under visible light. Dalton Trans 40(41):10822–10825
  91. Zhang H, Zhao L, Geng F, Guo L-H, Wan B, Yang Y (2016b) Carbon dots decorated graphitic carbon nitride as an efficient metal-free photocatalyst for phenol degradation. Appl Catal B 180:656–662
  92. Zhang J, Yu C, Lang J, Zhou Y, Zhou B, Hu YH, Long M (2020a) Modulation of Lewis acidic-basic sites for efficient photocatalytic H<sub>2</sub>O<sub>2</sub> production over potassium intercalated tri-s-triazine materials. Appl Catal B 277:119225
  93. Zhang L, Jin Z, Lu H, Lin T, Ruan S, Zhao XS, Zeng Y-J (2018) Improving the Visible-Light Photocatalytic Activity of Graphitic Carbon Nitride by Carbon Black Doping. ACS Omega 3(11):15009–15017
  94. Zhang P, Song T, Wang T, Zeng H (2017a) In-situ synthesis of Cu nanoparticles hybridized with carbon quantum dots as a broad spectrum photocatalyst for improvement of photocatalytic H<sub>2</sub> evolution. Appl Catal B 206:328–335
  95. Zhang X, Ren Y, Ji Z, Fan J (2020b) Sensitive detection of amoxicillin in aqueous solution with novel fluorescent probes containing boron-doped carbon quantum dots. Journal of Molecular Liquids: 113278
  96. Zhang Z, Yi G, Li P, Zhang X, Fan H, Zhang Y, Wang X, Zhang C (2020c) A minireview on doped carbon dots for photocatalytic and electrocatalytic applications. Nanoscale 12(26):13899–13906
  97. Zhang Z, Zheng T, Xu J, Zeng H, Zhang N (2017b) Carbon quantum dots/Bi<sub>2</sub>MoO<sub>6</sub> composites with photocatalytic H<sub>2</sub> evolution and near infrared activity. J Photochem Photobiol A 346:24–31

## Figures

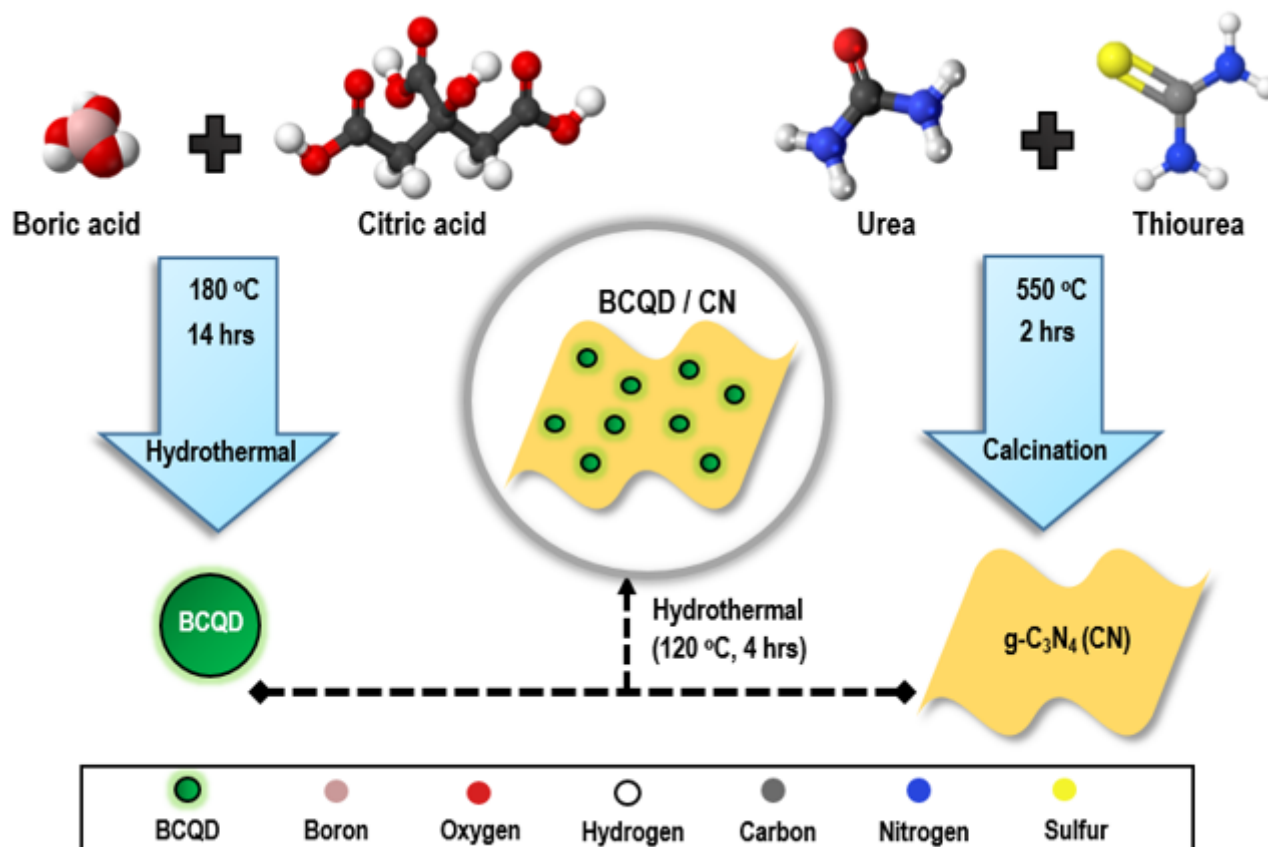
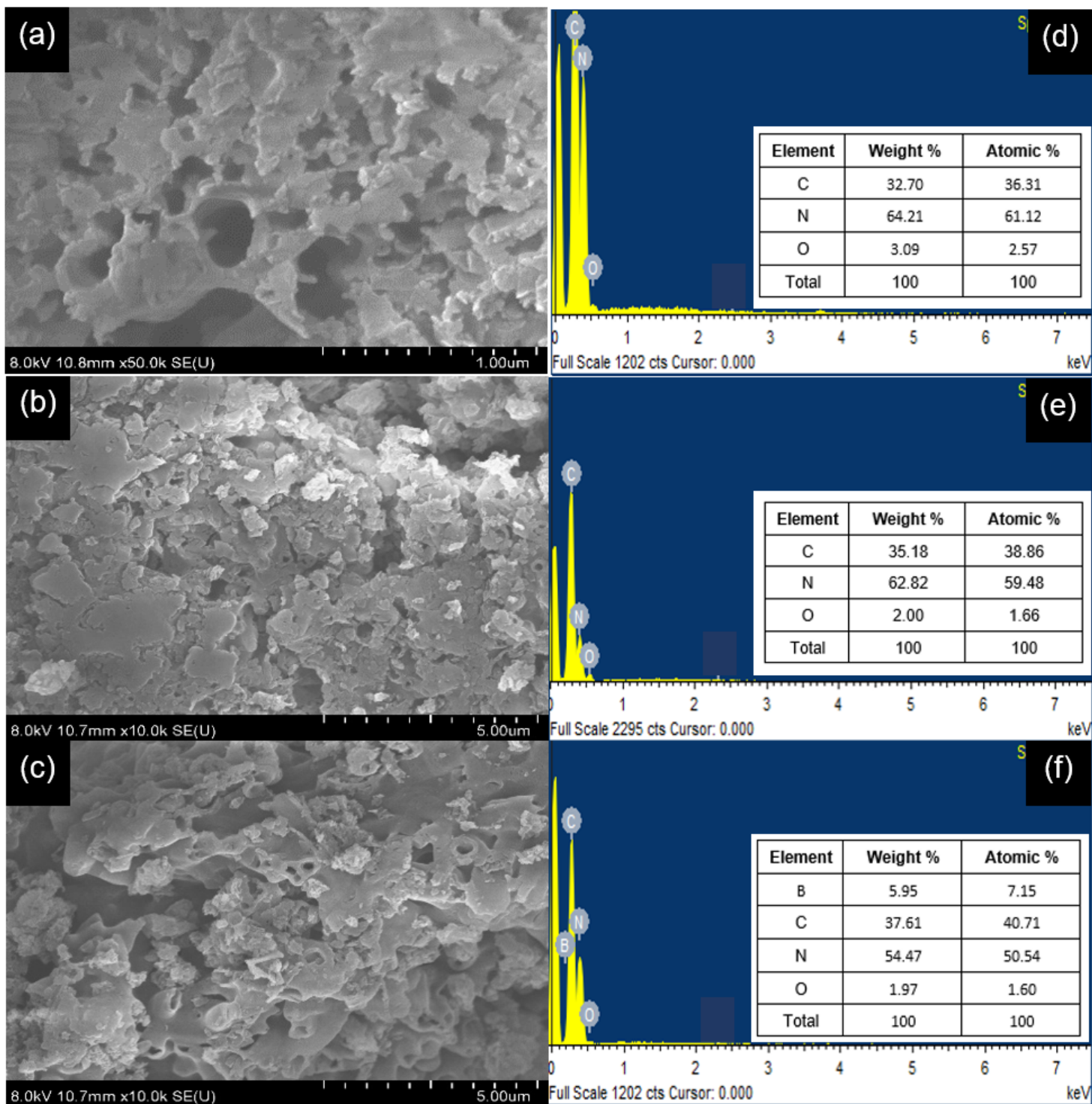


Figure 1

Schematic illustration of synthesis route for BCQD/CN nanocomposites



**Figure 2**

FESEM images of (a) CN, (b) CQD/CN and (c) 1-BCQD/CN, EDX spectra for elemental analysis of (d) CN, (e) CQD/CN and (f) 1-BCQD/CN

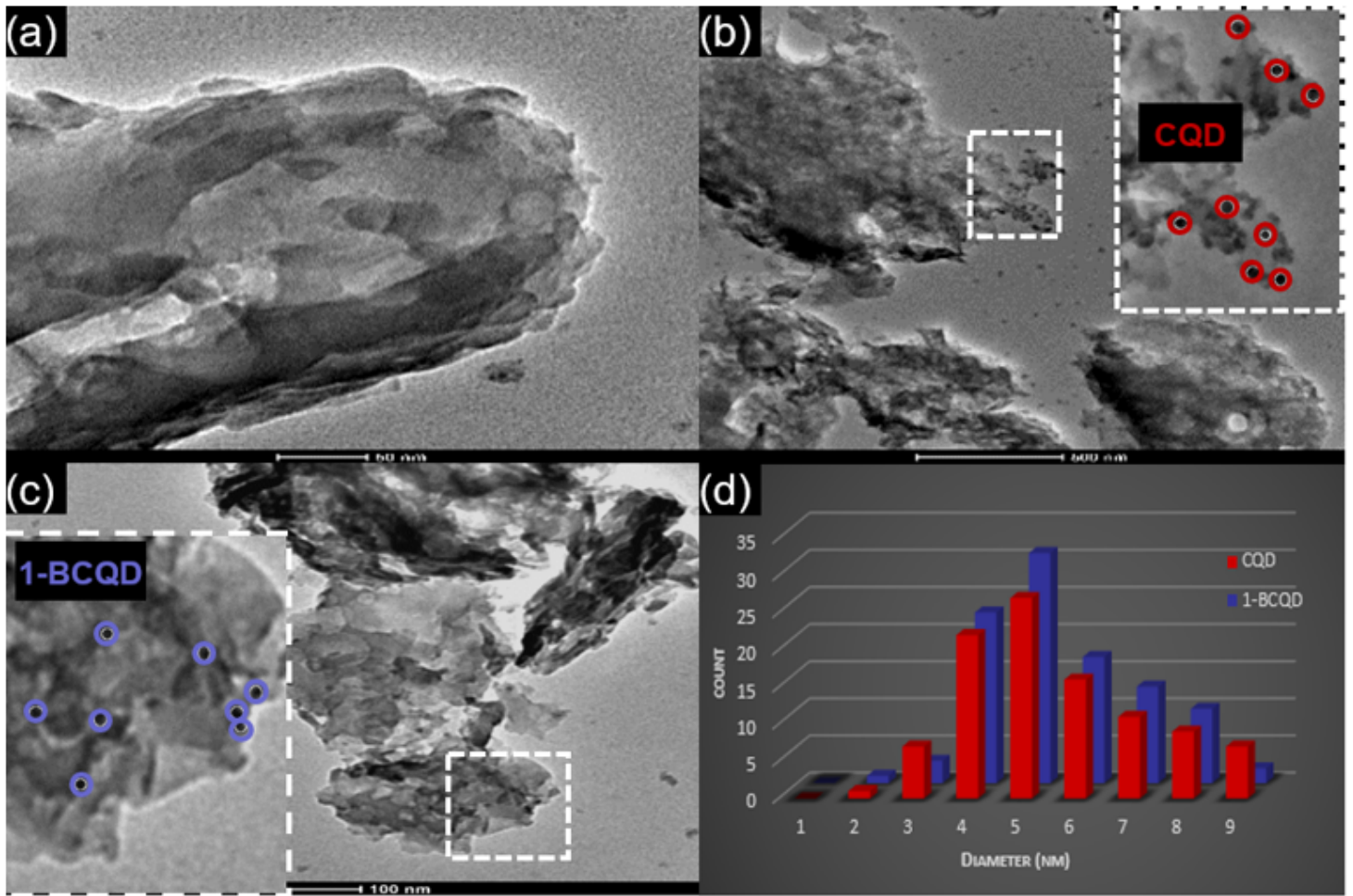


**Figure 3**

TEM image of (a) CN, (b) CQD/CN, (c) 1-BCQD/CN and (d) Particle size distribution of BCQD and CQD on 1-BCQD/CN and CQD/CN, respectively

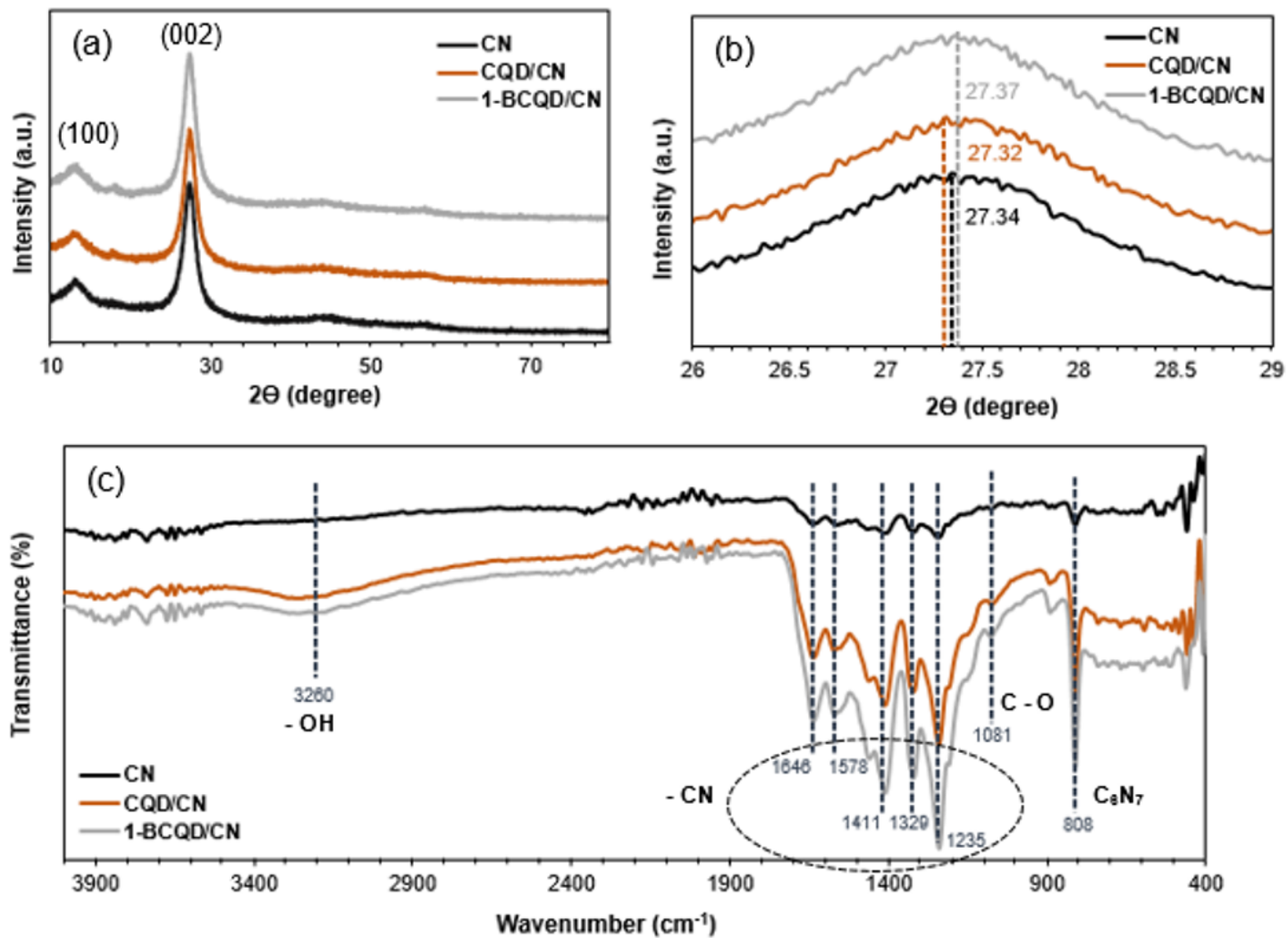
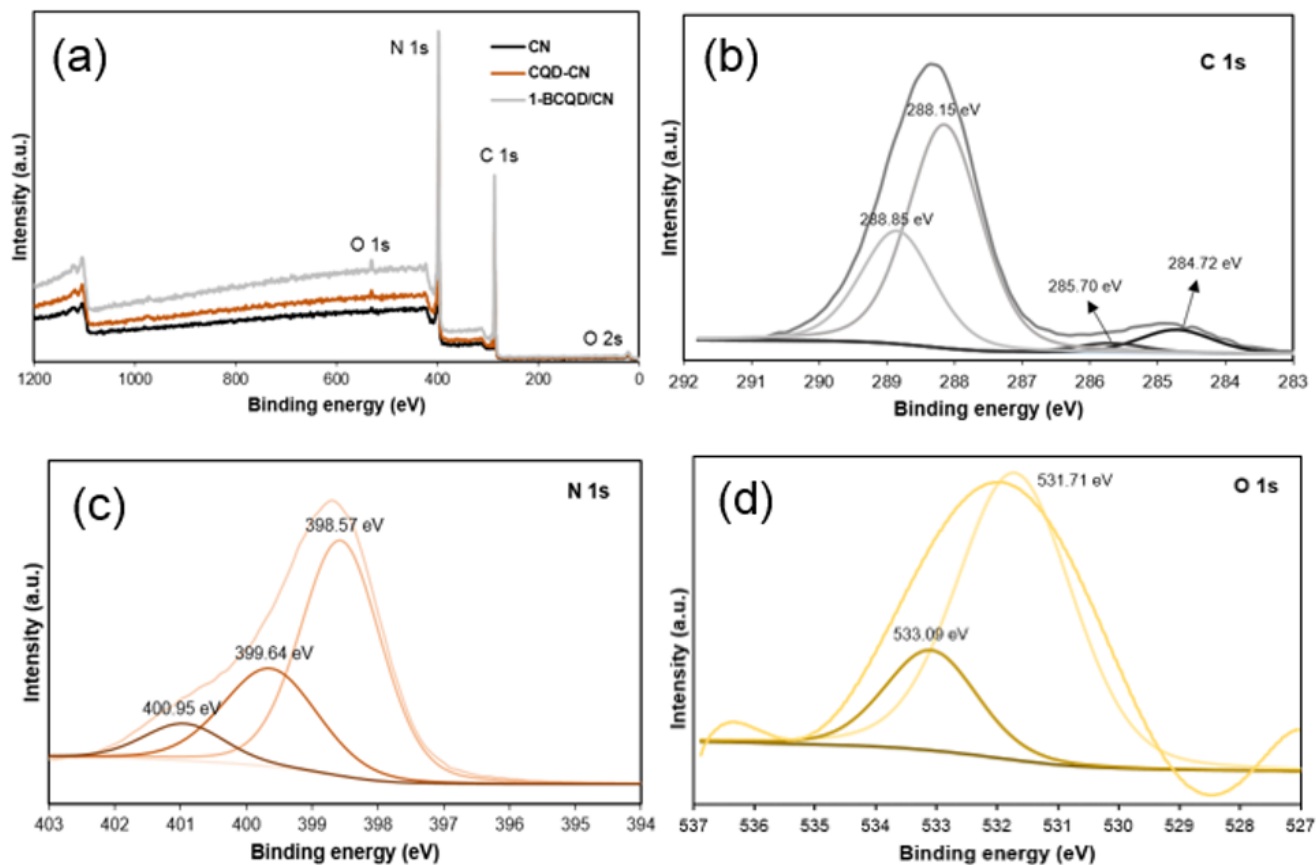


Figure 4

(a) XRD spectra, (b) Magnified (002) peak of the XRD profile and (c) FTIR spectra of CN, CQD/CN and 1-BCQD/CN.



(e)

Photocatalyst sample	Atomic percentage (At %)			Weight percentage (Wt %)		
	C 1s	N 1s	O 1s	C 1s	N 1s	O 1s
CN	38.67	59.90	1.43	35.02	63.26	1.72
CQD/CN	40.19	59.11	0.70	36.52	62.63	0.85
1-BCQD/CN	40.44	58.04	1.52	36.71	61.44	1.85

Figure 5

(a) XPS Survey spectra of CN, CQD/CN and 1-BCQD/CN; (b) C 1s spectra, (c) N 1s spectra and (d) O 1s spectra of 1-BCQD/CN; (e) Tabulated data of each element for CN, CQD/CN and 1-BCQD/CN

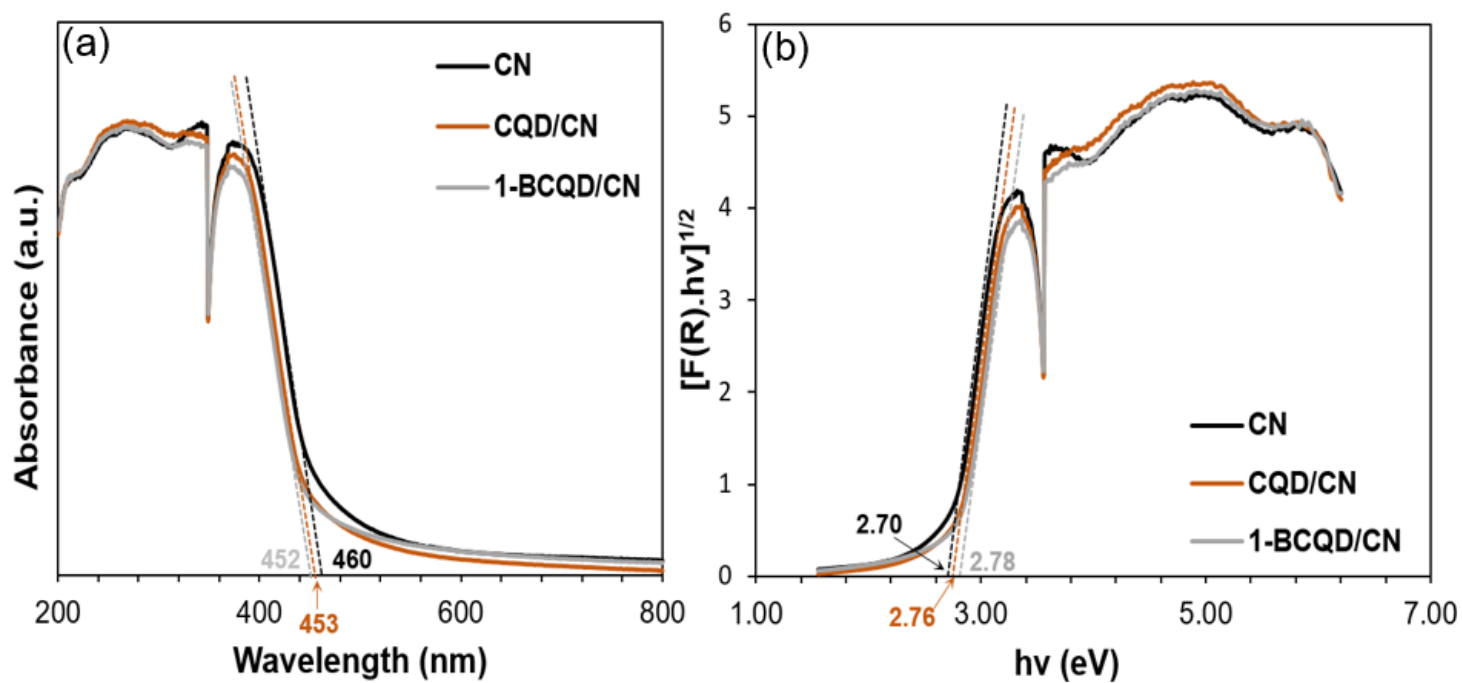
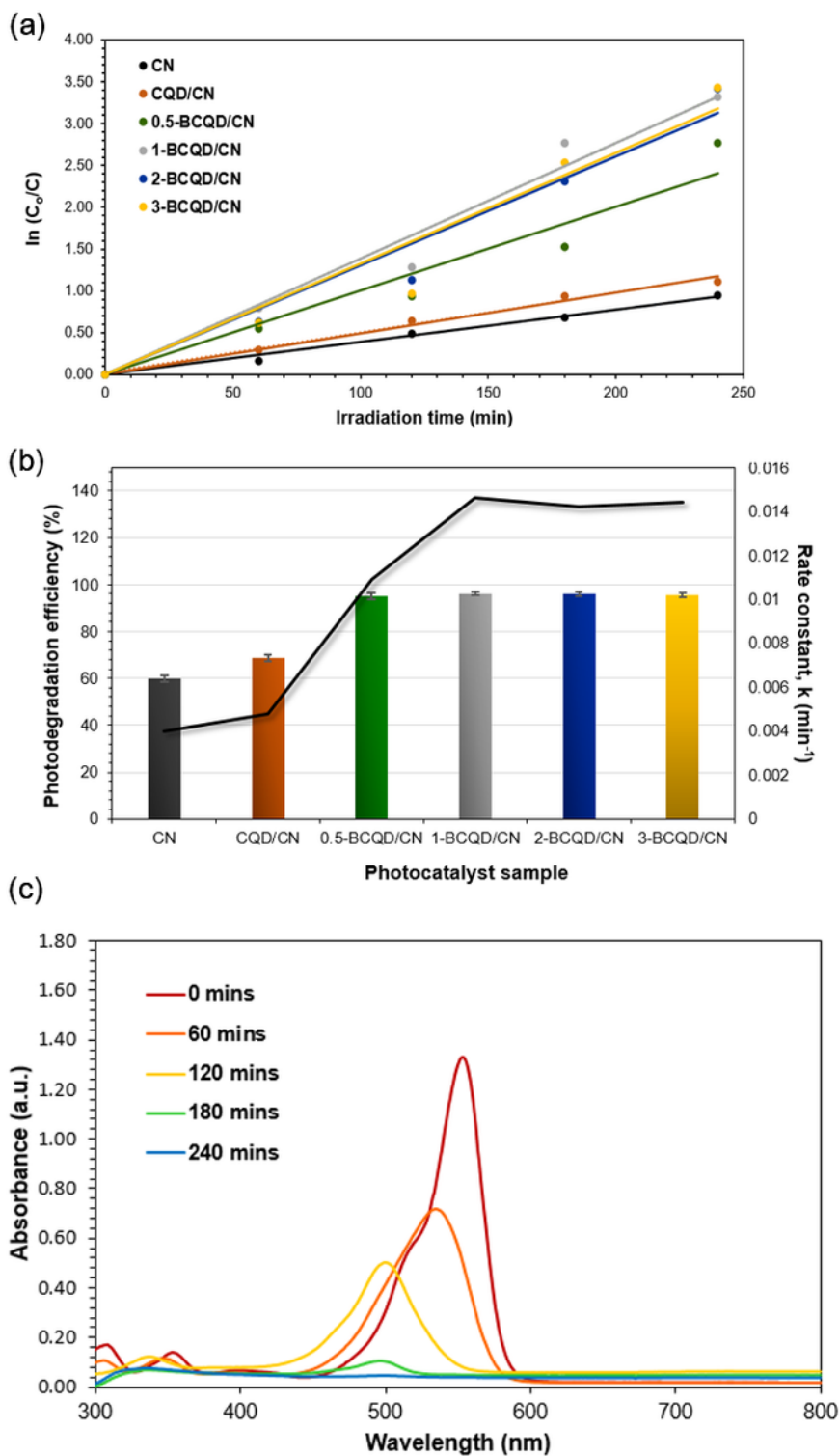


Figure 6

(a) UV-Vis diffuse reflectance spectra and (b) Corresponding Tauc plot of CN, CQD/CN and 1-BCQD/CN



**Figure 7**

(a) Linear graph of  $\ln(C_0/C)$  against irradiation time for all photocatalyst samples, (b) RhB degradation efficiency and kinetic rate constant of each photocatalyst under the irradiation of LED light and (c) Absorbance curves of 1-BCQD/CN at wavelengths between 300 and 800 nm for 240 mins with 60 min intervals (Inset: gradual decolorization of the RhB dye as a result of photodegradation in the presence of 1-BCQD/CN)

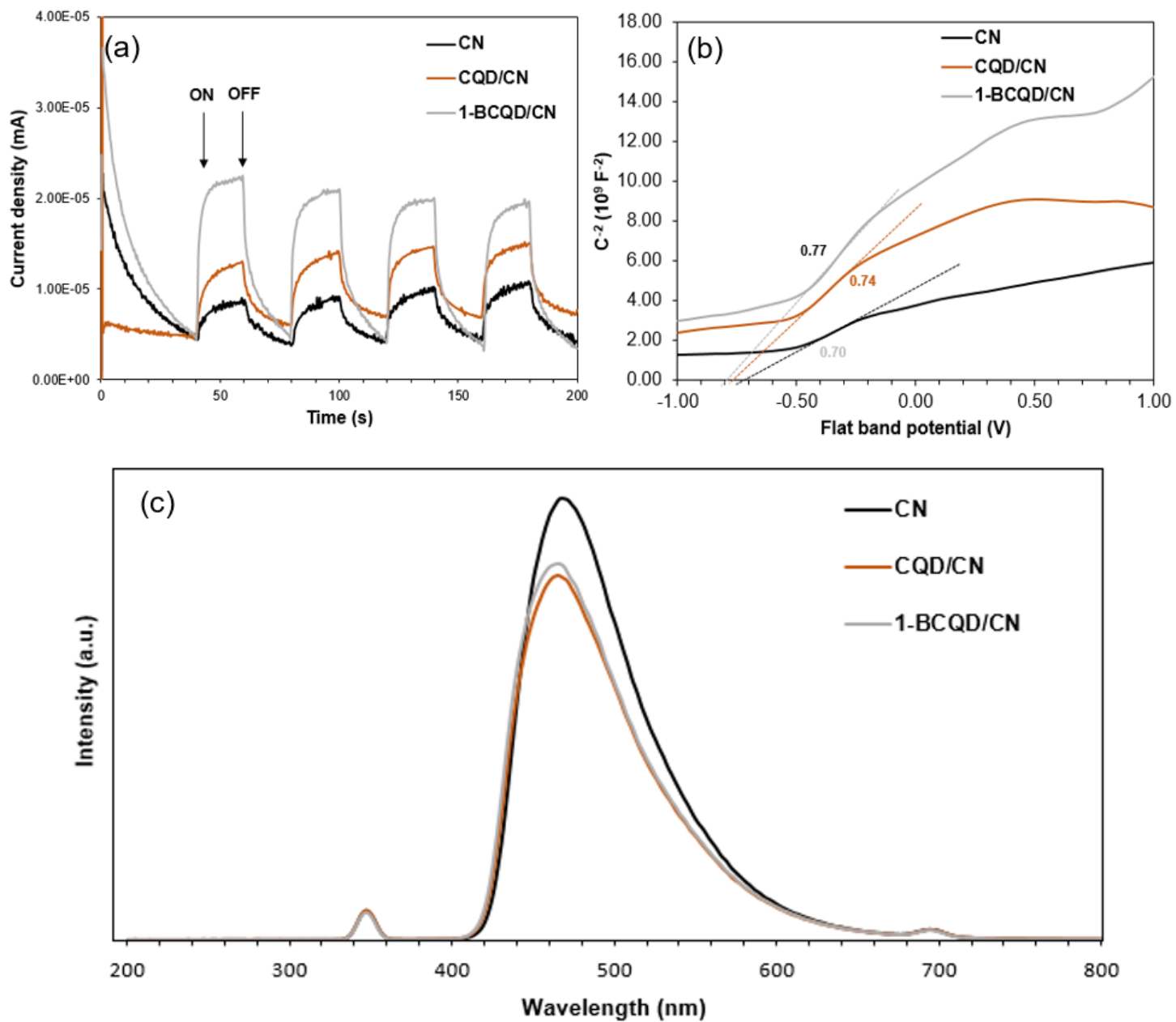


**Figure 8**

(a) Transient photocurrent response, (b) Mott-Schottky plots and (c) PL spectra of CN, CQD/CN and 1-BCQD/CN

(a)

Scavenger	Reactive species	C/C <sub>0</sub> at t = 240 mins	Degradation efficiency (%)
TEOA	h <sup>+</sup>	0.808	19.16
BZQ	·O <sub>2</sub> <sup>-</sup>	0.773	22.74
IPA	·OH	0.178	82.17
H <sub>2</sub> O <sub>2</sub>	e <sup>-</sup>	0.069	93.14
Without	N/A	0.032	96.77

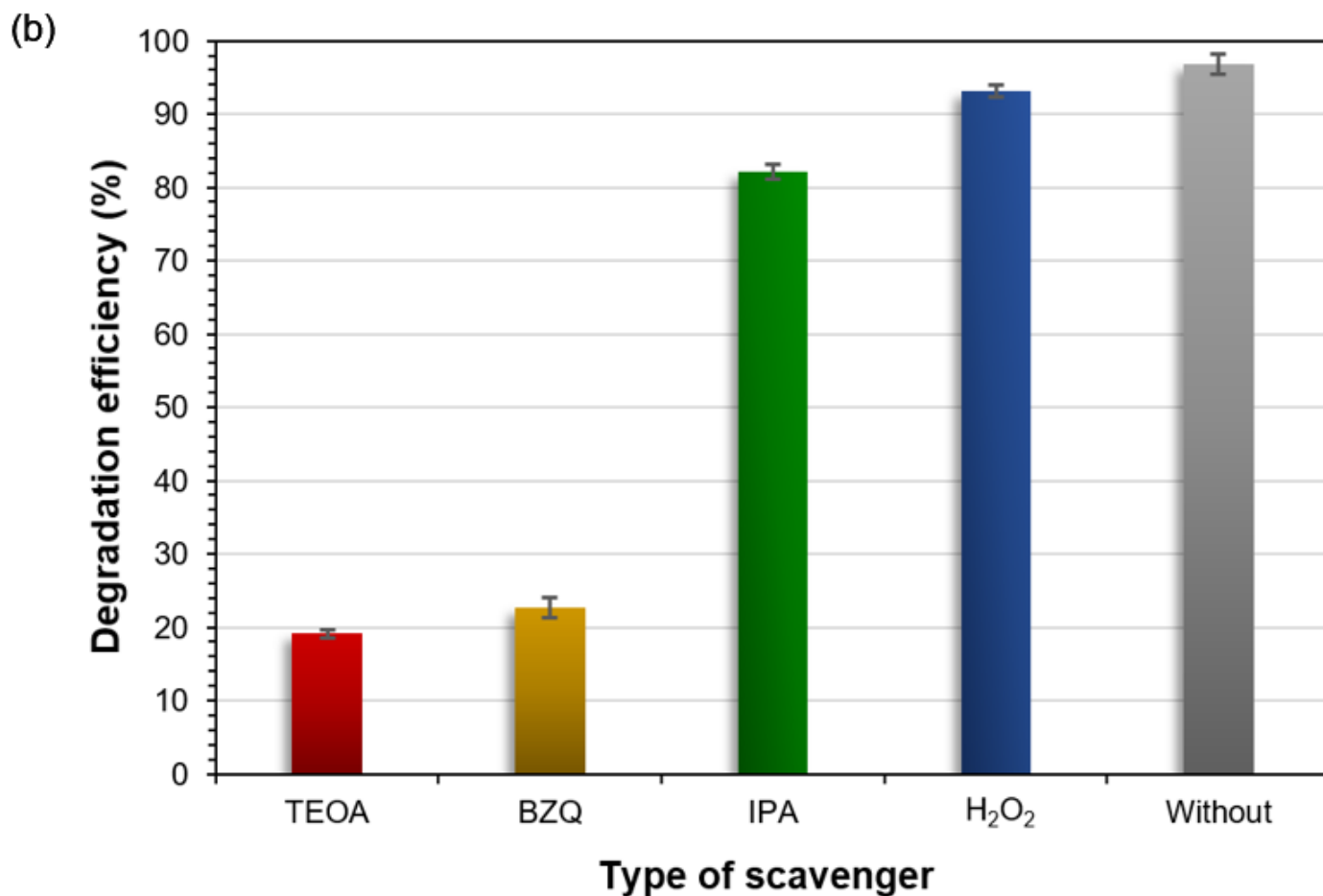


Figure 9

(a) Summary of photocatalytic performance and (b) Graph of photodegradation efficiency displayed by 1-BCQD/CN in the presence of different scavengers

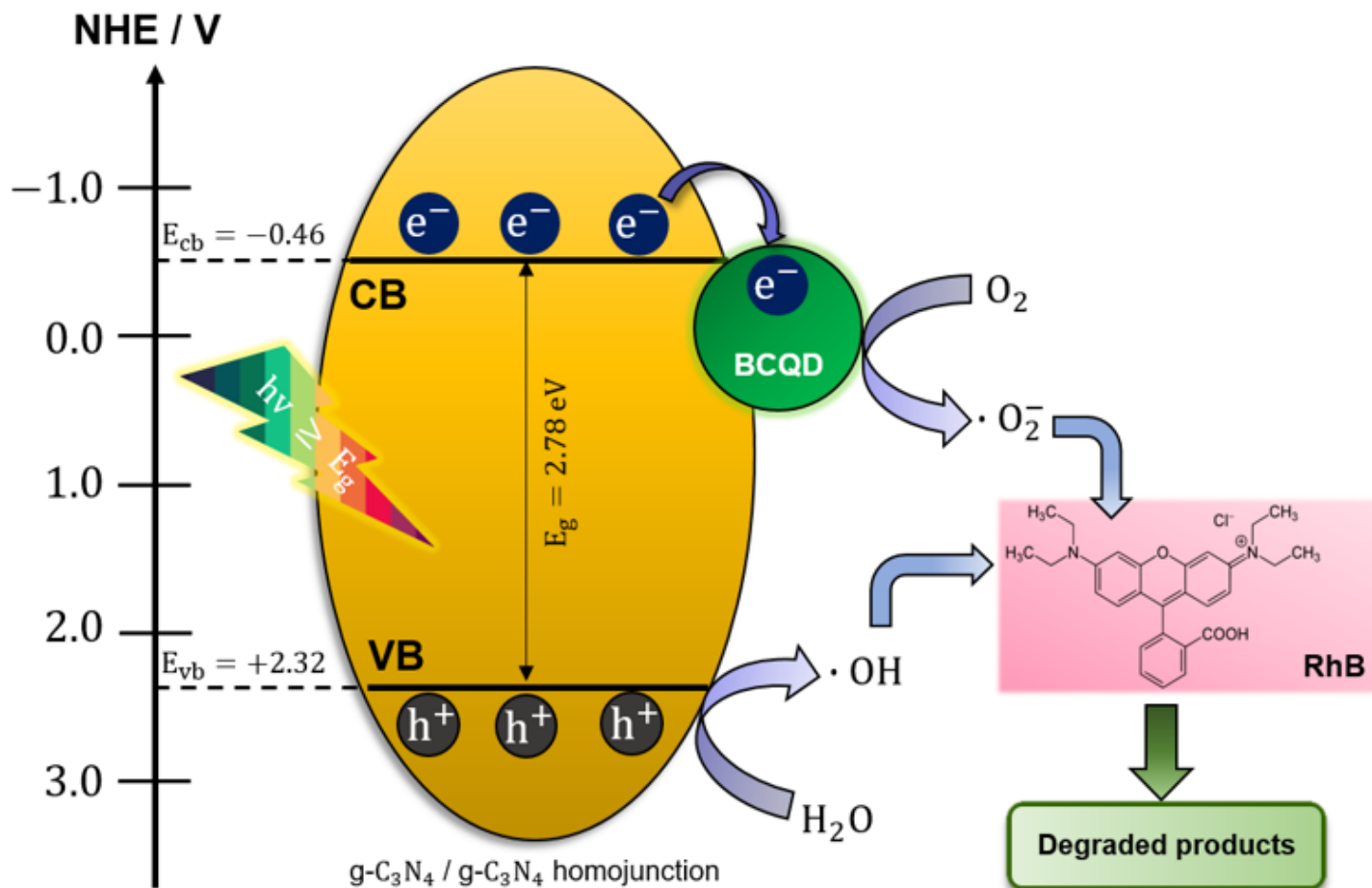


Figure 10

Schematic illustration of the plausible photocatalytic mechanism and a series of photo-reaction chain for RhB dye degradation in the presence of CQD-based g-C<sub>3</sub>N<sub>4</sub> as photocatalyst

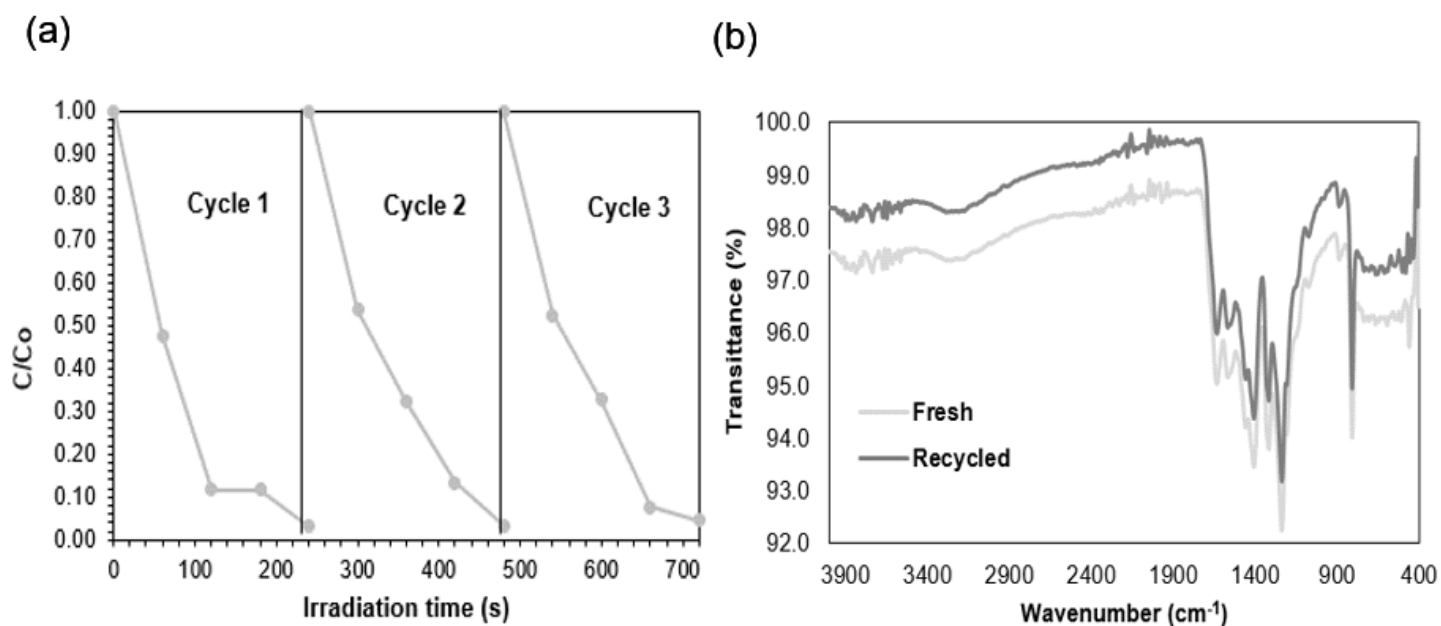


Figure 11

(a) Recyclability test of 1-BCQD/CN for 3 consecutive cycles and (b) FTIR spectra of 1-BCQD/CN in fresh and recycled conditions

## Supplementary Files

This is a list of supplementary files associated with this preprint. Click to download.

- [SupplementaryInformation.docx](#)